Universität Göttingen
Fakultät für Physik

Bachelorarbeit

Instabilities in driven granular matter
A bifurcation route to chaos

Instabilitäten in getriebener granularer Materie
Ein Bifurkationsweg ins Chaos

Sonka Reimers

September 8, 2014

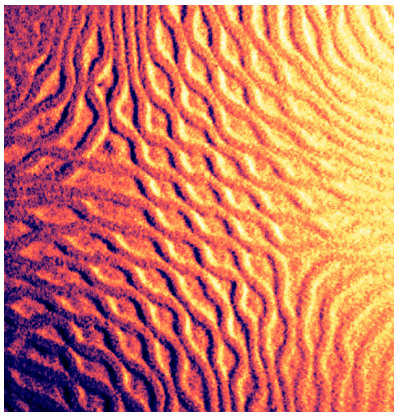

Erstgutachter: Dr. Marco G. Mazza
Zweitgutachter: Prof. Dr. Stephan Herminghaus
Institut für Nichtlineare Dynamik
MPI-DS, dep. DCF

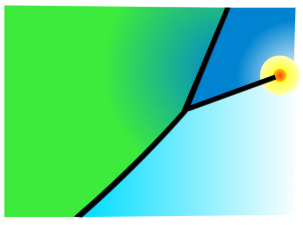

The cover picture shows a false-colour photograph of a pattern observed in shaking sand.

Contents

Abstract

Equilibrium is a state of maximal entropy or disorder; it "looks boring". In contrast, systems maintained far from equilibrium exhibit a diversity of fascinating behaviour including pattern formation and turbulence. These systems still pose fundamental questions.

In this thesis we report on a study of a granular, far-from-equilibrium system consisting of macroscopic, spherical particles confined in a narrow, cuboidal cell with a square base and large aspect ratio. The cell is vibrated sinusoidally in the direction perpendicular to the long sides. In previous work the system has been shown to behave as a two-dimensional granular gas. If the number of particles in the box exceeds a certain threshold, then we can observe several patterned states upon varying the driving amplitude. The patterns are found to consist of subharmonic standing waves reminiscent of Faraday waves in molecular fluids. We observe time-independent patterns as well as a spatiotemporally chaotic state in which the pattern changes its shape rapidly. At higher driving amplitudes impressive wave fronts sweep across the system and destroy the patterns. The waves are replaced by a large-scale circulation if the amplitude is increased further. These states show characteristics of turbulence. We ascertain that the system has no characteristic length-scale after descending into the turbulent state.

Chapter 1

Introduction

The diversity of patterns found in nature is breathtaking. Patterns can be observed in cloud formation, animal hides, ripples on sand and many other natural scenarios, see Fig. 1.1. During the last decades the study of pattern formation in laboratories developed into an important branch of nonlinear physics. Pattern-forming laboratory systems often show a transition to chaotic or turbulent behaviour upon a variation of the experimental parameters.

(a) (b) (c)

Figure 1.1: Patterns found in nature: (a) geological formations [1], (b) sand dunes [2], (c) giraffe fell marking [3].

In this thesis we report on the analysis of patterns formed in a granular system. The system studied consists of macroscopic, spherical, dry particles. The particles are confined in a narrow cuboidal cell with a square base. To agitate the particles the cell is vibrated vertically using an electromagnetic shaker. By varying the driving parameters (driving amplitude, A, and driving frequency, f) of the vibration,

we observe a sequence of patterns emerge in the system as well as a transition to states that show characteristics of turbulence. The patterns consist of standing waves oscillating at subharmonics of the driving driving frequency. The different patterned and turbulent-like states could be observed at different mean volume filling fractions[1], ϕ, driving frequencies, f, and for different cell geometries.

In this chapter we briefly introduce granular systems, pattern formation and turbulence including a short literature review to place our research in context. The subsequent chapter contains a description of the experimental methods and the apparatus. The driving amplitude of the electromagnetic shaker needed to be calibrated, the calibration process is described in Sect. 3. In the following chapter we briefly discuss a liquid-gas-like phase separation that can be observed in the system at low filling fractions. This work was carried out to familiarise myself with the apparatus. In Chap. 5 we present the measurements and observations of the pattern-forming behaviour and the transition to turbulent-like states. Section 5.4 contains quantitative evidence that the wave-like state of the system is indeed turbulence. We verify the oscillation frequency of the standing waves that form the patterns in Sect. 5.5. In the penultimate chapter we critically discuss the experimental imperfections of the apparatus and the methods used. The final chapter contains a summary of the thesis, an evaluation putting the results into context and comparing them to observations in different pattern-forming systems as well as ideas for future work.

1.1 Granular Matter

A granular material is an agglomeration of large numbers of solid, macroscopic particles. For macroscopic particles, the complex microscopic interactions between particles can be modelled as a simple contact interaction when two particles collide. Granular materials are dissipative systems. The collision of two particles is inelastic, that is the kinetic energy decreases upon every collision [4].

In practice one refers to granular systems even if other interactions are present but negligible and the particle-particle collisions dominate the behaviour. This

[1] We define the mean volume filling fraction as $\phi = NV_{\text{particle}}/V_{\text{cell}}$ here N is the number of particles in the cell, and V_{particle} and V_{cell} are the volume of one particle and the cell respectively.

yields a lower boundary for the particle size of approximately 100 µm, because for smaller particles van der Waals forces cannot be neglected. In principle no upper range for the particle size exists and the concept of granular matter may even be applied to such things as planetary rings [4].

Although the equations of motion determining the behaviour of each individual particle can easily be written down using classical mechanics, the collective behaviour of many-body systems like granular systems still lacks a theoretical basis. Granular matter behaves differently from any of the four classical states of matter: solid, liquid, gas and plasma. A granular system can show characteristic features of two or more states, but also exhibits unique behaviour. Consequently, granular matter is not only studied because of its wide application field in industry[2], but also for the fundamental questions it still poses [6, 7].

When the average kinetic energy of the particles is low and the motion of the particles relative to each other is small, the system acts like a solid. Granular solids can appear in disordered, glass-like, or highly ordered, crystalline states [7, 8]. If the mean kinetic energy is increased and the particles are allowed to flow, then a granular system behaves like a liquid and can be described by a hydrodynamical approach [7]. A further increase of the average kinetic energy in loosely confined systems leads to a transition to gas-like behaviour [7]. The transition from solid-like to liquid-like and gas-like behaviour can be observed experimentally [9–11]. Additionally, steady-state granular systems are known to separate into different phases. For example, in a certain parameter range, the system studied in this project is known to separate into a hot, dilute, gas-like and a cold, dense, liquid-like phase [9, 12]. A brief description of the phenomenon can be found in Chap. 4, for more details see [9, 12].

As granular systems dissipate energy through collisions, the system can only be in a steady state of a constant mean kinetic energy, if the dissipation is balanced by energy injection through an external source. One way to realise this is by vibrating or tapping the particles. By constantly injecting energy the system is maintained in a far-from-equilibrium state. Like other dissipative systems they exhibit a wide range of pattern formation (see Sect. 1.2). The pattern-forming

[2]Patrick Richard claimed: "Granular materials are ubiquitous in nature and are the second-most manipulated material in industry (the first one is water)" [5].

behaviour strengthens the analogy between granular systems and molecular fluids which show pattern formation in a great variety of different systems. In molecular fluid pattern-forming behaviour is extensively studied both theoretically and experimentally [13]. Before describing the patterns observed in granular systems we introduce the general principles of pattern formation in the next chapter.

1.2 Pattern Formation

Pattern-forming systems belong to a class of systems that are maintained out of thermodynamic equilibrium by an external "control parameter", such that the mechanisms which drive the system out of equilibrium compete against dissipative mechanism that restore equilibrium if the driving stops. The mechanisms that drive the system out of equilibrium could be a flux of momentum, energy or mass [13, 14]. Examples of a control parameter are a temperature gradient, a gradient in the chemical concentration or parametric forcing. The restoring, dissipative mechanisms can be viscous friction, heat conduction or diffusion [14].

Typically the system has some kind of basic, homogeneous state that looses stability if the control parameter passes a critical threshold. At this point, the homogeneous state is replaced by a patterned arrangement known as the "primary pattern" or "primary instability". Especially close to the instability threshold of the primary pattern, similar behaviour in very different systems can be observed [13, 14]. The primary pattern often shows no time-dependence and has a simple spatial structure.

A further variation of the control parameter can cause a transition from the primary pattern to another state where a new pattern forms, the secondary instability. In many cases secondary patterns are slight modifications of the primary pattern [13, 15]. Instabilities of tertiary and higher order can lead to a succession of time-independent and time-dependent patterns with growing complexity until the system transitions into a chaotic or sometimes turbulent state [14].

(a) (b) (c)

Figure 1.2: Examples of convective patterns observed in a Rayleigh-Bénard convection experiment with silicone oil. Image (a) shows a straight line pattern. Image (b) a zig-zag instability and image (c) a cross-roll instability. The cross-roll instability and the zig-zag instability have developed out of the straight line pattern. The images (a) -(c) are taken from [16].

Rayleigh-Bénard Convection

Rayleigh-Bénard convection ("RBC") is one of the simplest sustained nonequilibrium systems and one of the most studied examples of a convective pattern-forming system [17]. A general introduction to Rayleigh-Bénard convection is given in [13, 14, 18], recent developments are summarised in [19].

An RBC experiment consists of a layer of fluid between two horizontal plates. The bottom plate is kept at a warm temperature $T = T_1$, whereas the top plate is cold $T = T_2 < T_1$, so that fluid near the bottom plate is warmed with respect to that near the top plate. The flux of energy is the mechanism that drives the system out of equilibrium. The temperature difference ΔT (control parameter) creates a density gradient in the fluid, because the warmed fluid expands. The density difference results in a buoyancy force. For a small temperature difference, ΔT, viscous forces exceed the buoyancy force so that heat is transferred solely through heat conduction (restoring mechanism) from the bottom to the top plate. When the temperature difference exceeds a critical threshold $\Delta T \geq T_{\text{crit}}$ ("primary instability threshold"), the buoyancy forces exceed viscous forces and convection sets in. If ΔT remains close to the primary instability threshold, a steady flow forming a straight roll-pattern is established. With increasing temperature dif-

ference, the fluid can undergo instabilities of higher order, and various kinds of secondary patterns like zig-zag, skewed-varicose, wavy roll or crossroll instabilities (see Fig. 1.2), can be observed. When the temperature is increased further, the flow can lose its spatial or temporal coherence and becomes chaotic ("spatiotemporal chaos" see Fig.1.3). The system transitions into turbulence, often phrased as a "descending into turbulence", at even higher ΔT.

Figure 1.3: Snapshot of a spatiotemporally chaotic pattern, "Spiral Defect Chaos". The photograph shows a cylindrical Rayleigh-Bénard convection cell with CO_2-gas. The spiral structures move in time. The defects emerge randomly in the system and either merge with neighbouring spirals or disappear. The image is taken from [20].

In the "soft turbulent" state the flow exhibits random characteristics in space and time. If ΔT exceeds a certain, higher threshold, the coherence of the flow is restored and a large-scale circulation sets in [21–23]. This regime is referred to as "hard turbulence". Summarising: upon increasing the temperature difference the system undergoes various pattern-forming instabilities, exhibits spatiotemporal chaos and descends into soft and hard turbulence.[3]

Faraday Experiment

The Faraday experiment is a common example of a periodically forced pattern-forming system. For a brief introduction see [14]. Its basic element is a layer of fluid in a container that is shaken vertically with a fixed frequency and amplitude.

[3]To the extent of my knowledge, in the literature there is no clear distinction between behaviour labelled as spatiotemporal chaos and that labelled as turbulent. A turbulent regime is also spatiotemporally chaotic, but a spatiotemporally chaotic regime is not necessarily turbulent; for example, it is not necessarily characterised by the absence of a typical length scale.

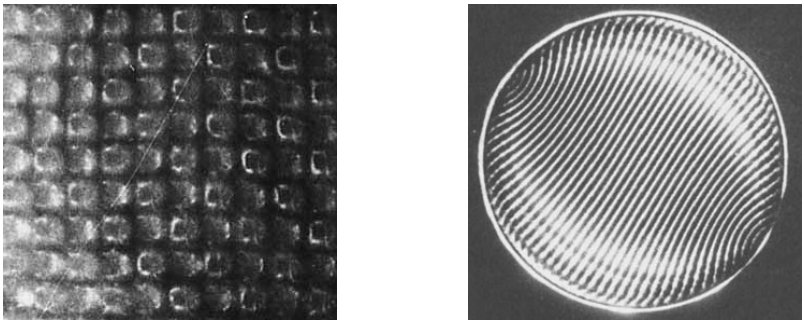

(a) (b)

Figure 1.4: Primary patterns observed in Faraday waves with single-frequency forcing: In low-viscous fluids squares (a) emerge, whereas in high-viscous fluids stripes (b) form. Panel (a) shows a Faraday experiment with oil in a rectangular cell at a forcing frequency $f = 20\,\mathrm{Hz}$. The primary pattern emerges as nearly perfect squares. The image is taken from [24]. A pattern of essentially parallel lines is observed with high-viscous fluid, a mixture of 88 % glycerol and 12 % water at a forcing frequency $f = 80\,\mathrm{Hz}$. The image is taken from [25].

If the acceleration exceeds a critical threshold the flat surface of the fluid becomes unstable and standing surface waves can be observed oscillating at subharmonics of the driving frequency, f. These surface waves are known as "Faraday waves", named after Michael Faraday who first described them in an appendix to an article in 1831 [26].

The shape of the surface wave depends on the properties of the fluid. Close to the primary instability threshold, low-viscous fluids typically develop a square pattern, whereas in high-viscous fluids stripe pattern, analogous to the straight roll patterns in RBC, can be observed [25]. Higher instabilities include hexagonal lattice patterns [14, 25]. Figure 1.4 shows examples of patterns observed in Faraday experiments. The surface waves of primary instabilities oscillate at half the driving frequency, that is the period doubles with respect to the homogeneous state. With increasing driving acceleration faraday systems can show a sequence of period doublings, that is patterns oscillating at $f/4$, $f/8$..., before the system descends into a turbulent regime [14, 15].

Multiple frequency forcing allowed to discover a great variety of different patterns and "quasi-patterns"[4][25].

[4]Quasi-patterns are analogous to two-dimensional quasicrystals. A quasicrystal describes a

Pattern Formation in Granular Systems

During the last decades pattern formation in granular matter has been observed and studied experimentally, numerically and theoretically in two- and three-dimensions. A detailed review can be found in [7]. Various types of patterns in different cell geometries have been reported [29–34].

To our knowledge, all reported experiments of the pattern formation process in granular media were carried out in open-top or very high cells, in which a shaking bottom plate injects energy and drives the particles and gravity acts as a confining force keeping the system together [31, 32, 35, 36]. If the driving acceleration exceeds a critical threshold, then the flat surface of the granular layer becomes unstable and a standing wave oscillating at a subharmonic of the driving frequency f appears. Figure 1.5 illustrates the structure of the pattern showing a side-view of a standing wave. Figure 1.6 shows examples of patterns (top-view) including squares, stripes and hexagons observed in a granular bed. The patterns oscillate at $f/2$ and $f/4$ respectively. Other investigations have revealed localized excitations ("oscillons") [37], as well as spiral patterns [31], crossroll patterns [38] and skew-varicose patterns [38] which look strikingly similar to patterns observed in Rayleigh-Bénard convection. Like the Faraday experiment, the granular system is an example of a periodically forced pattern-forming system undergoing surface instabilities. In both the granular and molecular fluid systems the patterns appear as a surface instability. Additionally some patterns observed in granular systems (squares, stripes, hexagons) are strongly reminiscent of patterns observed in the Faraday experiment. It is important to note differences between the systems: In the molecular fluid, surface waves with a dispersion relation $f(k)$ exist in the absence of external forcing, and the forcing amplifies the modes with $f(k)$ close to subharmonics of the driving frequency. In the granular system surface waves cannot exist without external forcing (indeed the system does not remain in the fluid-like state without the external forcing) and the driving frequency does not fix the wavenumber of the patterns [28].

Although several instabilities of higher order have been studied in granular systems and a period-doubling route has been observed [28, 34, 39], turbulent

structure that is ordered but not periodic [27].

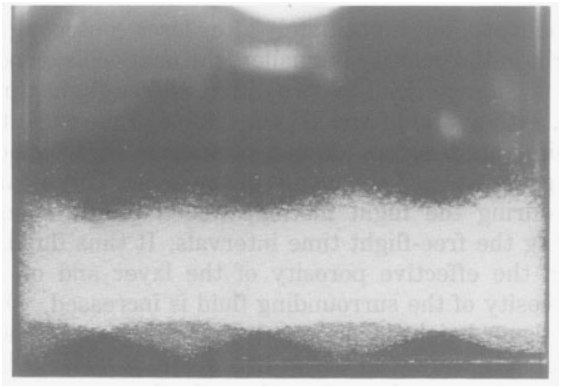

Figure 1.5: Side-view of standing waves taken from [28]: "Photograph of the grain layer, stroboscoped at the excitation frequency. The double-period motion is clearly visualized by the two superposed shapes, indicating four regions of the layer oscillating successively out of phase."[28]

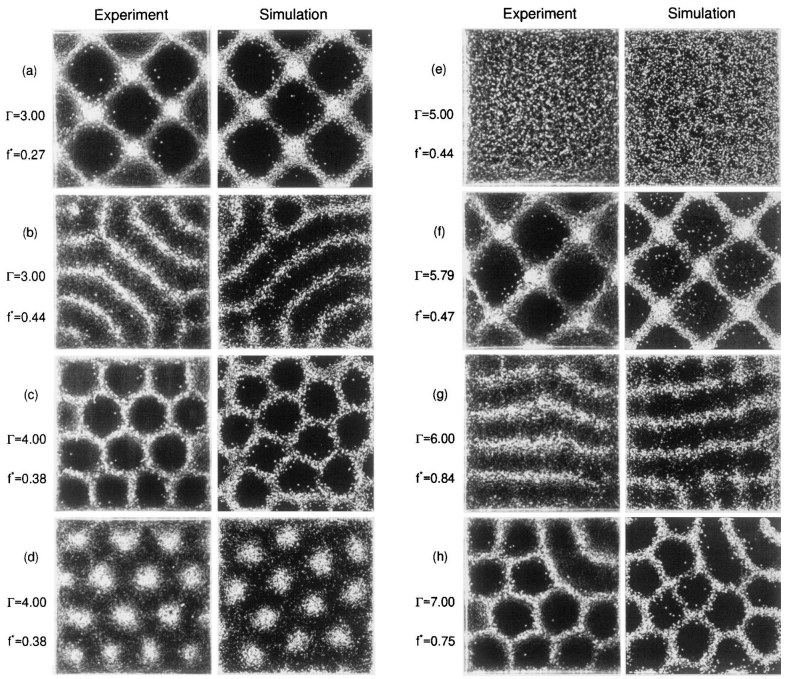

Figure 1.6: Standing wave patterns observed in experiment (left) and simulation(right) of driven granular matter [29]. Γ indicates the dimensionless driving acceleration $\Gamma = A(2\pi f)^2/g$, here A, is the driving amplitude, f the driving frequency and g the gravitational acceleration. The patterns are described as: "(a) squares, (b) stripes, (c) and (d) alternating phases of hexagons, (e) flat layer, (f) squares, (g) stripes, and (h) hexagons. Patterns (a) - (e) oscillate at $f/2$, (f) - (h) at $f/4$. The dimensionless layer depth $[n]$ is 5.42. The brightness indicates the height of the layer. The experiments use lead spheres sieved between 0.5 and 0.6 mm."[29]

states have only been observed in simulations of two-dimensional systems [40–42].

1.3 Turbulence

Our understanding of turbulence was first based on observations in molecular fluid dynamics. Turbulence is a flow regime characterised by chaotic changes in various observables and rapid fluctuations. A turbulent flow is highly irregular, it is often characterised by vortex generation. Compared to laminar flow, turbulent flow is highly diffusive ("good mixing properties") and highly dissipative ("high rates of kinetic energy are converted into heat") [43].

Several attempts have been made to develop a theoretical model for turbulence in molecular fluids: The phenomenology is usually phrased in terms of "eddies", vortex-like structures. Turbulence causes the formation of eddies of many different length scales. Figure 1.7 shows two examples of turbulent flow. In Fig. 1.7 (a) the three-dimensional vortex generation in the turbulent flow of a free jet is illustrated. Figure 1.7 (b) shows a quasi-two-dimensional turbulent flow observed in Jupiter's atmosphere. As the images illustrate, two- and three-dimensional turbulence looks (in general) significantly different from each other [43].

In three-dimensional turbulence, it is usually assumed that energy is injected in large-scale structures and "cascades" towards smaller length scales in the so-called "inertial range" until the structures are small enough that the energy is dissipated through viscous mechanisms. Based on this energy cascade and the assumption of self-similarity, Kolmogorov proposed a first phenomenological theory for the energy transfer in the inertial range [46]. According to this theory the cascade is independent of the fluid properties and the nature of the energy injection. The theory predicts that the energy spectrum of the velocity field $E(k)$, follows a power-law $E(k) \sim k^{\alpha}$, where k denotes the local wavenumber. The power-law dependence reflects the assumption of scaling invariance, in this case self-similarity at each length-scale. In subsequent work the theory was refined and further theories were developed predicting a power-law dependence of the energy spectrum. The literature reports an exponent of $\alpha = -5/3$ (Kolmogorov-Obukhov (KO) scaling) for the range in which inertial forces dominate [46]. If instead buyoncy forces dominate, then an exponent of $\alpha = -11/5$ (Bolgiano-Obukhov

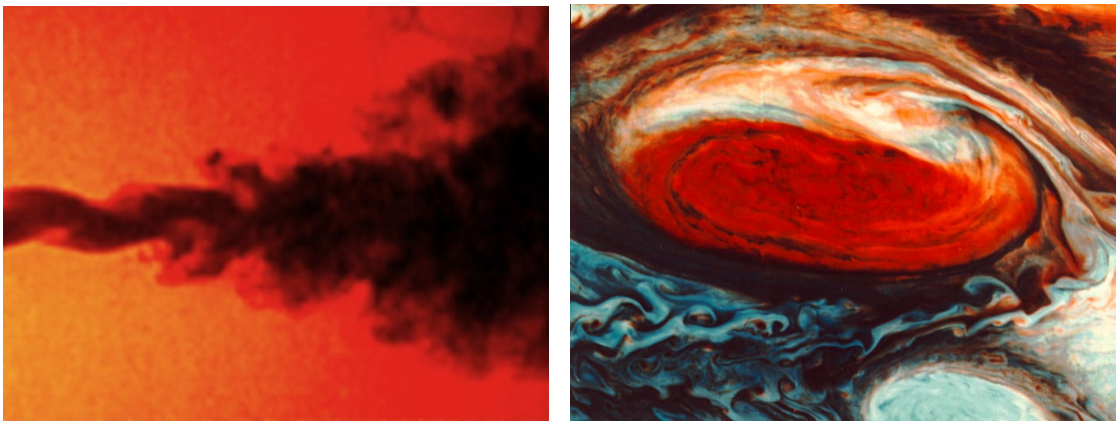

(a) 3D (b) 2D

Figure 1.7: Three- and two-dimensional turbulence. Panel (a) shows the three-dimensional vortex generation of a free jet. At the left hand side of the photograph, the flow is still laminar, but smoothly transitions into turbulence at the right hand side. Panel (b)shows a quasi-two-dimensional turbulent flow: A false colour image of Jupiter's Great Red Spot. The large-scale vortex is characteristic of two-dimensional turbulence. The images are taken from [44] (a) and [45] (b), respectively.

(BO) scaling) is predicted [47, 48].

Two-dimensional turbulence is extremely different. Through eddy-cannibalisation large-scale structures develop out of small scale structures [43]. In 1967 Kraichnan [49], Leith [50] and Bachelor [51] pioneered the theoretical study of two-dimensional turbulence based on Kolmogorov's concept for three-dimensional turbulence. The theory is based on the assumption that the forcing injects energy and enstrophy in a narrow band of intermediate length scales and that energy is transferred to larger length scales, an "inverse cascade", and all enstrophy flows downscale to smaller length scales, "direct cascade" [43, 52]. The Kraichnan-Leith-Batchelor ("KLB") theory predicts a power-law scaling of the energy spectrum $E(k)$ with a scaling exponent of $\alpha = -5/3$ in the upscale energy range and $\alpha = -3$ in the downscale enstrophy range with a possible logarithmic correction [53]. To our knowledge, clear evidence of the coexistence of the two cascades on an extended range has not been reported yet [54]. As Bofeta *et al.* [54] point out, the inverse energy cascade has been observed in many experiments (for example [55]), and in numerical simulations (for example [56–58]). For the direct cascade earlier

numerical simulations (for example [59]) and experiments [60] show spectra slightly steeper than KLB's prediction of $\alpha = -3$ [54]. More recent investigations (e.g. [61, 62]) report on spectra closer to the prediction $\alpha = -3$ [54]. It has been shown that a large-scale drag force, which is always present in experiments, requires a correction to the exponent -3 [63].

Although turbulence has already been studied by Leonardo Da Vinci in the years 1508–1513 [64] and especially in the last century much research has been done on this subject, a complete description of turbulence remains one of the most significant unsolved problems in modern physics[5] [66].

[5]The problem is also listed as one of the Millenium Prize Problems in mathematics [65].

Chapter 2

Methods and Experimental Apparatus

The experiments are carried out in a closed, cuboidal cell with a square base. The cell contains an approximately monodisperse sample of dry, spherical bronze particles. Using dry particles and preventing electric charging, we ensure, that long-range particle interactions are negligible so that the behaviour is dominated by the contact forces when two particles collide. To agitate the particles, the cell is placed on the head of an electromagnetic shaker that vibrates vertically. Figure 2.1 shows a photograph and a sketch of the apparatus.

2.1 Main Components

Below, we briefly describe the main components of our experimental apparatus.

Particles

Throughout this work, we use dry, spherical, bronze particles. The density of bronze is $\rho = 8900\,\mathrm{kg\,m^{-3}}$ and collisions of bronze particles can be modelled by a coefficient of restitution of $\varepsilon = 0.7$ [29].

The diameter of the particles is in the range $180\,\mu\mathrm{m} < d < 200\,\mu\mathrm{m}$. The size of the particles was controlled by sieving them. In order to check the shape, the particles were rolled on sand paper. Nearly spherical particles roll on the paper,

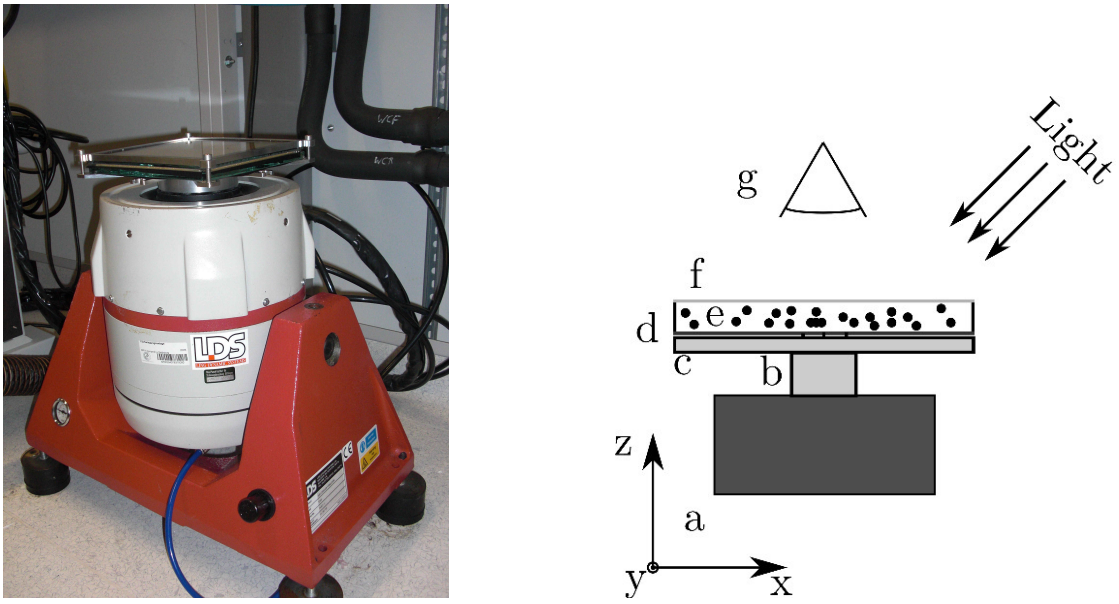

(a) (b)

Figure 2.1: Photograph (a) and sketch (b) of the experimental set-up (side view). In panel (b) the letters denote: a. the electromagnetic shaker, b. the head of the shaker, c. the substructure, d. the bottom plate and the side walls, e. the bronze particles, f. the top glass plate, g. the position of the observer/camera. The arrows indicate the lighting. The cell is shaken vertically (z-direction) and observed through the top plate from above, parallel to the driving.

whereas particles of irregular shape stick to it. Sticky particles were picked out manually. The remaining particles were examined under a microscope.

To remove residual moisture from the surface of the particles, the particles were washed with two solvents, isopropanol and ethanol and dried in an oven at 200 °C for approximately 45 min. Before every experimental run the particles were rolled in an aluminium tray so that the grains could discharge. Figure 2.2 shows a photomicrograph of randomly chosen particles.

Cells

The cells are rectangular cuboids with square base areas and large aspect ratios $\gamma = L_0/h$; here h denotes the height and L_0 the side length of the cell. In total three cells with two different aspect ratios $\gamma_b > \gamma_s$ were used: Two large cells C_3,

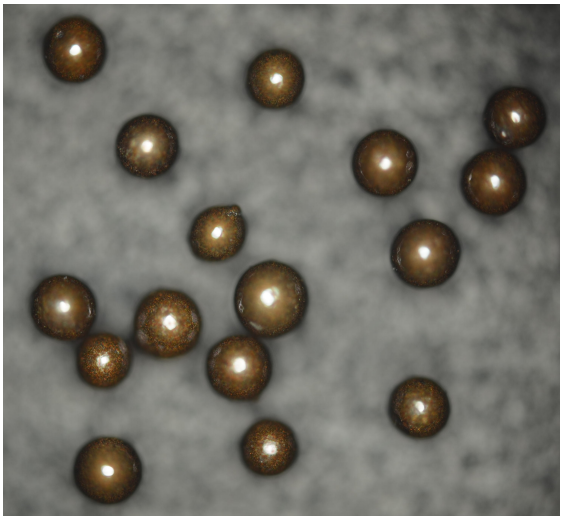

Figure 2.2: Photomicrograph of randomly chosen particles taken with tenfold magnification.

C_1 ($\gamma = \gamma_\mathrm{b}$) and a small cell C_2 ($\gamma = \gamma_\mathrm{s}$). An overview of the different geometries is given in Tab. 2.1.

The height of every cell is $h = 3\,\mathrm{mm} \approx 15.8\,d$. The side lengths of the small and the large cells are $L_0 = 75\,\mathrm{mm}$ and $L_0 = 180\,\mathrm{mm}$ respectively. Each cell consists of four main components: a bottom plate, the sidewalls, a glass top plate (lid) and a frame that holds the system together. The bottom plates are metallic in order to prevent electric charging.[1] The cell is connected to the shaker via a star-shaped substructure that can be bolted directly to the head of the electromagnetic shaker. One arm of the substructure is extended so that an accelerometer can be attached. It is desirable to make the system as light as possible, because the strength of the shaker is limited.

Large Cell C_1

Figure 2.3 shows a sketch and a photograph of the large cell C_1. Except for the glass top plate, all components are made out of duraluminium, an age-hardening aluminium alloy. Duraluminium was chosen because of its high rigidity and low

[1] We used a glass bottom plate in preliminary experiments, because glass plates are typically flatter than metal plates, but for high driving accelerations the particles charged up very quickly and stick to the glass.

	h/mm	$\mathbf{L_0}$/mm	γ	**comment**
C_1	3	180	60	corners with curvature of finite radius
C_2	3	75	25	sharp corners
C_3	3	180	60	sharp corners

Table 2.1: Overview of the geometry of the different cells. All cells are rectangular cuboids with square base.

density. The thickness of the square bottom plate is $h_{\mathrm{bp}} = 5\,\mathrm{mm}$, the side lengths are $L_{\mathrm{bp}} = 22.4\,\mathrm{cm}$ each. At the outer edges the height of the bottom plate is reduced by 1 mm over a 1.2 cm wide stripe. The one-piece sidewalls are slot to this indent such that the inner horizontal dimension of the cell is $L_0 = 18\,\mathrm{cm}$. The side walls are screwed to the substructure with two screws on each side. The 6 mm-thick top glass plate is slot on an indent of the sidewalls at the top inner edges. The glass plate is locked into position by a frame that rests on the edges of the top plate and can be screwed to the sidewalls on each side thus holding the system together. At each corner screws running from the frame, through the sidewalls and the bottom plate into the substructure, provide additional fixing of the cell components and fix them to the substructure. Several holes are milled in the substructure and the sidewalls to reduce the weight of the system. Figure A.1 in the appendix shows the different components of the large cell C_1 in detailed engineering sketches.

To prevent cracks in the glass, the edges of the glass plate are covered with one layer of rubber adhesive tape. For the same purpose the screws at the side walls need to be tightened before the screws at the corners, because the screws in the corners can create significant tension in the glass.

The particles are very sensitive to vibrations and irregularity in the driving of the cell. Therefore the bottom plate is fixed to the substructure with double-sided tape, which was found to be useful to damp vibrations. Additionally, close to the head of the shaker, small screws run from the substructure to the bottom plate. These screws were added to ensure the contact between the double-sided tape, the substructure and the bottom plate. As inhomogeneities in the bottom plate can affect the behaviour of the particles severely, the screw holes in the bottom plate are only 2.5 mm deep so that the 3.5 mm-thick top region of the bottom plate is

undisturbed.

It is important that all components fit flush to each other, because any gap broader than the particle diameter is likely to cause a particle leakage. To ensure

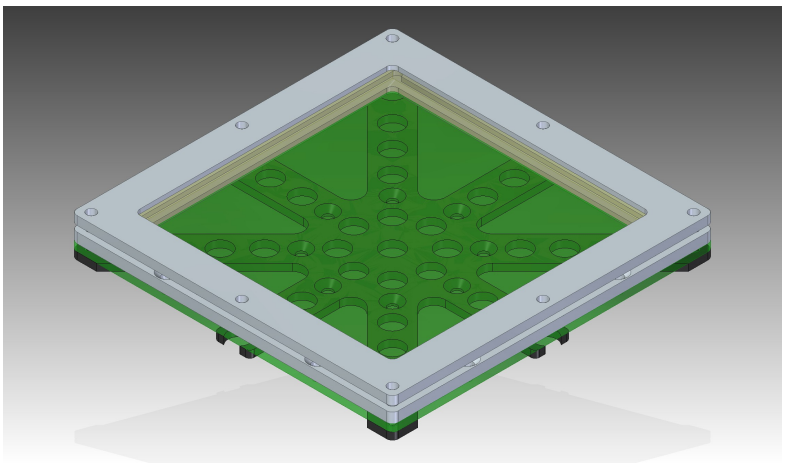

(a)

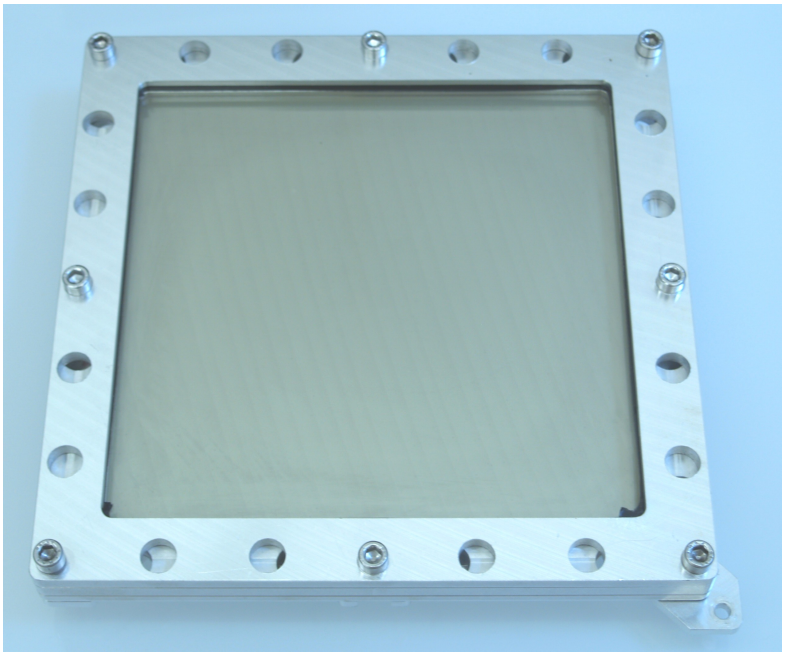

(b)

Figure 2.3: Sketch (a) and photograph (b) of the large cell C_1. In panel (a) the bottom plate is shown in transparent green. It is placed on the star-shaped substructure. Between the one-piece sidewalls and the frame a glass plate is placed.

the precision of less than 100 µm in the manufacturing process, the corners of the cell are not sharp, but have a curvature of finite radius.

Small Cell C_2

The small cell C_2 is considerably smaller in size. This allows to use material of higher density and thicker plates without exceeding the limit of the mass that the shaker can drive. This cell consists of a steel bottom plate and a glass top plate. Both plates are 10 mm-thick. The plates are separated by 3 mm-thick glass stripes that are glued to the top plate and serve as the side walls. They form sharper corners. The cell is held together by a steel frame that rests on the edges of the top plate. At the corners the frame is screwed onto a steel substructure similar to the one of the large cell C_1. This set-up does not require additional screws between the substructure and the bottom plate, because the smaller, thicker system is more stable and less likely to flex. Images of the small cell C_2 and the substructure are shown in Fig. 2.4.

Large Cell C_3

The early measurements were carried out in a preliminary set-up similar to the small cell C_2, but made out of duraluminium instead of steel and of inner dimensions equal to the inner dimensions of the large cell C_1. Compared to the cell C_3, the refined set-up C_1 is considerably more rigid and stable when shaken. Additionally, the amount of particles lost when filling or emptying the cell is significantly reduced in cell C_1.

Electromagnetic Shaker

The electromagnetic shaker is shown in Fig. 2.1. It drives the cell in the vertical direction perpendicular to the long sides. The vertical movement of the head of the shaker is controlled by a signal generator. The frequency f, the peak-to-peak voltage difference ("input voltage"), ΔU_{in}, and the shape of the signal can be modified. We choose a sinusoidal signal such that the vertical position of the cell can be described as

$$z(t) = A \sin(2\pi f t + \varphi_0) + z_0 \ . \tag{2.1}$$

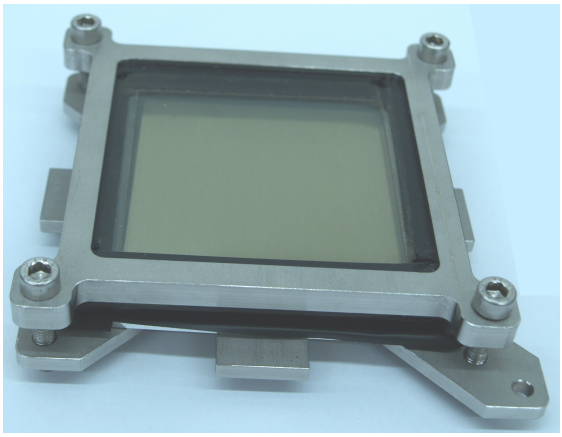

(a)

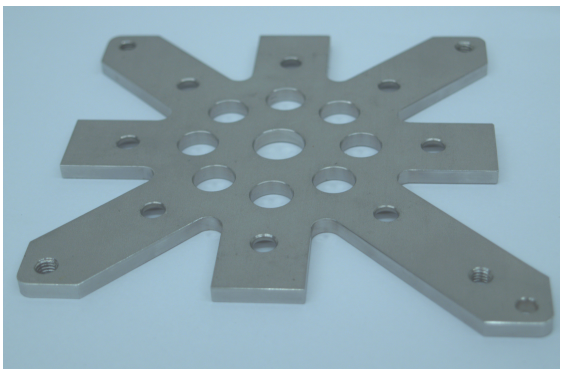

(b)

Figure 2.4: (a) Photograph of the small cell C_2. (b) Photograph of the substructure of the small cell C_2. An accelerometer can be attached to the extended arm of the substructure.

Converting the peak-to-peak voltage ΔU_{in} into the shaking amplitude, A, requires additional calibration (see Chap. 3).

The shaker is four-footed. The height of each foot can be changed by turning it. To avoid a drifting motion of the shaker, heavy rubber mats are placed underneath each foot. This is important because the floor is not sufficient flat to ensure that the system remains level if the shaker moves.

2.2 Camera and Image Analysis

To take photographs of the system, a camera was placed above the cell. Photographs are taken with a `Olympus Digital E-500` camera or a high-speed `PCO.1200s` camera. The frame rate of the high-speed camera is $500\,\mathrm{s}^{-1}$. High-speed photography requires significant lighting, we use a 500 W halogen flood light. Due to the inhomogeneous nature of the lighting, the images show a considerable intensity gradient. To remove this gradient, for every pixel the mean value of the corresponding column and row is subtracted.

2.3 Method

Taking measurements requires additional preparation: (i) The top and bottom plate of the cell are cleaned with two solvents, ethanol and isopropanol; (ii) an anti-static spray is applied to the glass top plate to help avoid static charging. Before the cell is put together, the spray must be dry. (iii) The particles are weighed out and rolled in an aluminium tray, so that the grains can discharge. In the tray the particles are inspected visually, any wet-looking material and dirt is picked out using tweezers.

If the grains get stuck to the internal structure of the electromagnetic shaker, they can severely damage the solenoid. Therefore a vacuum cleaner is used to ensure that no particles from the cell remain on the surface of the shaker.

The behaviour of the system is very sensitive to a tilt of the cell. Any slope results in a density gradient in the particles that adds additional weight to one corner and thus is likely to cause an avalanche. A steady state with homogeneous filling is therefore only possible in an extremely carefully levelled cell. The levelling changes slightly when the cell is driven, so that the levelling must be carried out when the electromagnetic shaker is switched on at the target driving amplitude and frequency. To level the cell, the feet of the shaker are turned.

At the beginning of each measurement the particles are to be distributed homogeneously throughout the cell. This is realized by driving the system at a high amplitude and exposing it to some amplitude modulation.

2.4 Parameters

We characterise our measurements in terms of the driving frequency, the driving amplitude and the mean volume filling fraction of the cell. The driving frequency of the shaker is the frequency of the input signal, but the driving amplitude cannot be obtained directly from the input voltage, ΔU_{in}. The conversion of the input voltage into the driving amplitude is described in Sect. 3. Typically we express the amplitude in terms of the particle diameter, d. We define the mean volume filling fraction as

$$\phi = NV_{\text{particle}}/V_{\text{cell}} \,,$$

where N is the number of particles in the cell, and V_{particle} and V_{cell} are the volume of one particle and the cell respectively. The mean volume filling fraction is related to the total mass, M, of all particles in the cell via the particle's density: $M = \rho\phi V_{\text{cell}}$. To check for the loss of particles, we measured the weight of the particles before and after the experiment and found that we can control the mean filling fraction within an experimental error of $\delta\phi = 0.5\,\%$.[2] The frequency is assumed to be error free. The error in the amplitude can be estimated by the precision of the signal generator $\delta U_{\text{in}} = 1\,\text{mV}$. The calibration process introduces an additional, systematic error in the amplitude of approximately $5\,\%$.

[2] It is nearly impossible to fill and empty the cell without loosing particles; $\delta\phi = 0.5\,\%$ refers to the large cell C_3 and the small cell C_2. If using the large cell C_1, the error is less than $\delta\phi = 0.05\,\%$.

Chapter 3

Calibration of the Electromagnetic Shaker

The vertical position of the head of the shaker is controlled by a signal generator. We require the shaker to reproduce the shape of the signal faithfully such that a sinusoidal input signal $U_{\mathrm{in}}(t)$ of frequency f_{in} creates a sinusoidal shaking of the same frequency $f_{\mathrm{shak}} = f_{\mathrm{in}} =: f$. The amplitude of the shaking A_{shak} is controlled by the peak-to-peak voltage difference of the input signal which we call the "input voltage" ΔU_{in} . The relation $A_{\mathrm{shak}}(\Delta U_{\mathrm{in}})$ depends on the mass that is shaken. The total mass of the particles M_{p} is small compared to the mass of the cell M_{c}, that is $M_{\mathrm{p}} < M_{\mathrm{c}}$, so that for each cell the relation $A_{\mathrm{shak}}(\Delta U_{\mathrm{in}})$ is independent of the filling fraction.

The calibration process consists of two steps:

1. A known input voltage ΔU_{in} is converted with an accelerometer into an output voltage ΔU_{out} which is directly proportional to the acceleration Γ of the cell. We define the output voltage ΔU_{out} as the peak-to-peak voltage difference of the accelerometer signal. For the output voltage ΔU_{out} Eq. (2.1) yields the relation $\Delta U_{\mathrm{out}} = \alpha\Gamma = \alpha A_{\mathrm{shak}}(2\pi f)^2$, $\alpha = \mathrm{const.}$

2. The output voltage of the accelerometer needs to be converted into SI units and then into amplitudes. The constant of proportionality between the voltage and the acceleration needs to be ascertained experimentally, because the value given in the handbook of the accelerometer is known to be wrong.

The conversion $\Delta U_{\text{in}} \rightarrow \Delta U_{\text{out}}$ depends on the cell (mass) shaken, whereas the constant α needs to be ascertained only once.

3.1 Step 1: $\Delta U_{\text{in}} \rightarrow \Delta U_{\text{out}}$

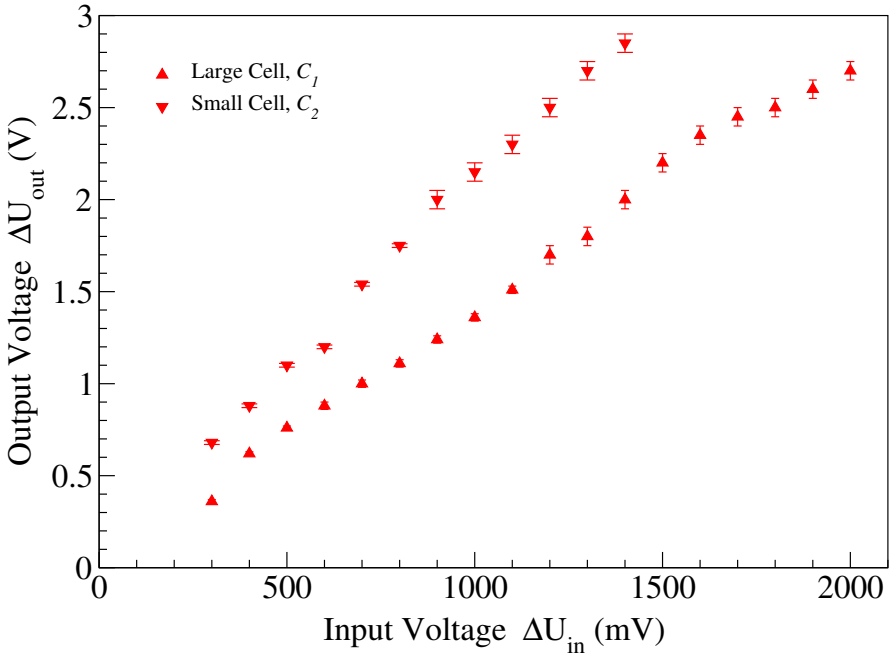

Figure 3.1: Dependence of the acceleration of the maximal input voltage difference of the signal generator ΔU_{in} for the large cell C_1 (upward triangles) and the small cell C_2 (downward triangles) at driving frequency $f = 100\,\text{Hz}$. The peak-to-peak voltage difference of the accelerometer ΔU_{out} is directly proportional to the peak acceleration.

The following procedure was carried out with the large cell C_1 and the small cell C_2. If the values for C_1 and C_2 are identical, only one value is given, otherwise the values in brackets always refer to the small cell C_2. The accelerometer was fixed at the extended arm of the substructure and its output was connected to an oscilloscope. The cell was shaken at different input voltages ΔU_{in}. The input voltage was varied between $\Delta U_{\text{in}}^{\text{min}} = 300\,\text{mV}$ and $\Delta U_{\text{in}}^{\text{max}} = 2000\,\text{mV}(1800\,\text{mV})$ in steps of 100 mV. For every ΔU_{in} the output voltage ΔU_{out} was read from the oscilloscope. The driving frequency was kept constant at $f = 100\,\text{Hz}$.

The results are shown in Fig. 3.1. The error bars correspond to one scale

gradation of the oscilloscope and show the experimental precision of the oscilloscope read-off. For both the small cell C_2 and the large cell C_1 ΔU_{out} increases approximately linearly with ΔU_{in}, but the slope of the curves differs significantly.

By repeating the measurements with the large cell C_1 at another driving frequency $\tilde{f} = 60\,\text{Hz} < f = 100\,\text{Hz}$, we verified that the relation $\Delta U_{\text{out}}(\Delta U_{\text{in}})$ is frequency-independent, that is the peak acceleration depends only on the mass to be shaken and not on the frequency.

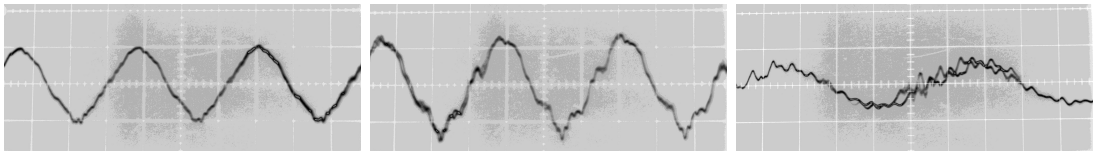

(a) 100 Hz, 1400 mV (b) 100 Hz, 1900 mV (c) 60 Hz, 800 mV

Figure 3.2: Photographs of the display of the oscilloscope showing the output voltage of the accelerometer. The accelerometer was attached to the shaking large cell C_1. The numbers under the panels indicate the input parameters f [Hz] and ΔU_{in} [mV] of the signal generator. For all images one scale unit of the oscilloscope corresponds to $\delta U = 1\,\text{V}$.

Figure 3.2 shows three photographs of the display of the oscilloscope - the accelerometer measurement - for the large cell C_1 at three different driving parameters. They illustrate that the sinusoidal signal is affected by considerable noise. The noise was found to increase with decreasing driving frequency and increasing input voltage.

Calibration of the large cell C_3

The accelerometer cannot be attached to the substructure of the cell C_3. Consequently the process described above could not be carried out with the this cell. To calibrate measurements taken in the large cell C_3, the measurements of the lowest amplitudes of the different states (see Sect. 5.2) taken in the large cell C_3 were repeated in the small cell C_2.

3.2 Step 2: $\Delta U_{\text{out}} \rightarrow A_{\text{shak}}$

To calibrate the voltage from the accelerometer the shaking amplitude was measured directly from sequences of images recorded using the high-speed camera.

Experimental Procedure

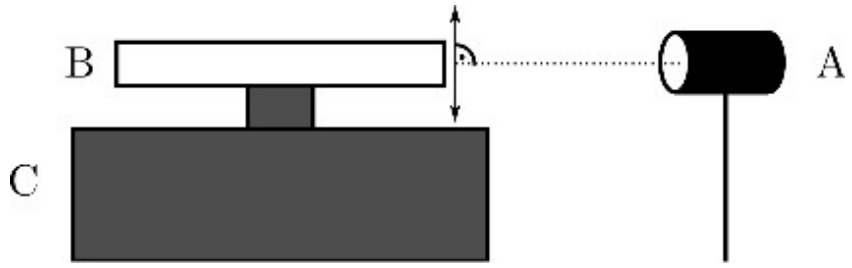

Figure 3.3: Sketch of the experimental set-up used for the calibration of the accelerometer; the letters denote A: high-speed-camera, B: large cell C_1, C: electromagnetic shaker. The arrow indicates the shaking direction and the dotted line the viewing direction of the camera.

The large cell C_1 was mounted on the shaker and the high speed camera placed such that the viewing direction of the camera was perpendicular to the shaking direction of the cell. The set-up is sketched in Fig. 3.3.

Sequences of 800 images were taken of the shaking cell using the maximum frame rate of $f_{\text{cam}} = 500\,\text{s}^{-1}$. The shaking frequency was kept constant at $f = 100\,\text{Hz}$. For each data set the amplitude was varied between $\Delta U_{\text{in}} = 300\,\text{mV}$ and $\Delta U_{\text{in}} = 1800\,\text{mV}$ in steps of 100 mV for $\Delta U_{\text{in}} \leq 1000\,\text{mV}$ and in steps of 200 mV for $\Delta U_{\text{in}} \geq 1000\,\text{mV}$. Additionally one image of a static cell was taken. The position of the camera and the shaker were not changed during the calibration procedure.

Data Analysis

For every image sequence we used a bright line on the cell to mark the vertical position of the cell (see Fig. 3.4). A sinusoidal regression of the position versus time was carried out to determine the amplitude of the shaking. The amplitude measured from the images in pixel was converted into metric units according to the following procedure.

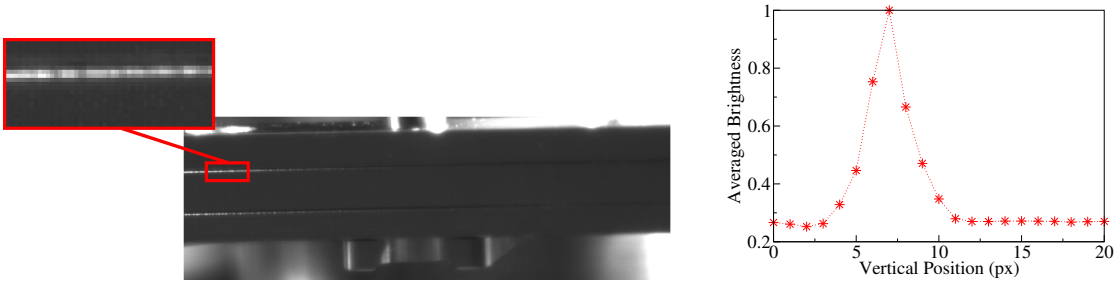

(a) (b)

Figure 3.4: (a) Image of the static cell as taken for the measurements of the vertical position. The region marked red shows the area to which the images of the driving cell were cropped. The position of the cell is measured by identifying the position of the bright horizontal line (the line separating the frame from the sidewalls) in the cropped images. (b) Horizontal average of the brightness plotted against the vertical position. The data were normalised such that the maximum value equals unity. The maximum of this curve corresponds to the position of the line separating the frame from the sidewalls.

(1) The images are cropped such that the image section shows only a part of the substructure and the sidewalls (see Fig. 3.4). The separating line appears bright in the image and is approximately horizontal in this image section. Therefore we ascertain the vertical position of the line by identifying the maximum of the horizontally averaged intensity for each image section.

(2) We assume that the position of the cell in time t can be described as

$$z(t) = A\sin(2\pi f t + \phi_0) + B \ , \tag{3.1}$$

here A denotes the shaking amplitude that is to be determined, B represents a vertical offset, ϕ_0 to a phase shift and $f \approx 100\,\text{Hz}$ to the frequency.

To account for any errors or irregularities in the shaking frequency or the frame rate of the camera f is used as a free parameter. For the same reason we do not fit one curve to the whole dataset at once. Instead, we carry out multiple regressions and limit the fitting range of an individual regression to two full shaking periods (0.02 s, 10 images). In steps of $\Delta t = 0.002\,\text{s}$ (1 data point), the position of the fitted range is moved from the first two shaking periods to the last two full cycles. The regressions are carried out using the `fit`-command provided by `gnuplot`. The resultant values of A and f are stored for every regression.

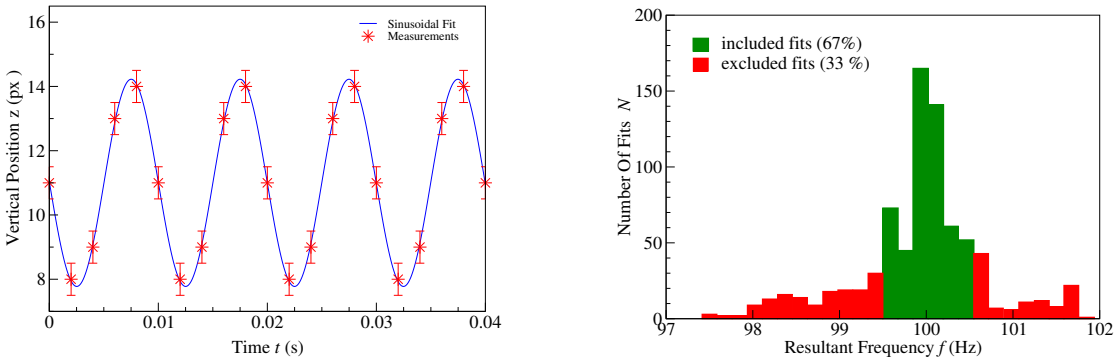

(a) (b)

Figure 3.5: (a) Vertical position of the large cell C_1 driven at $f = 100\,\text{Hz}$ and an input voltage of $\Delta U_{\text{in}} = 1400\,\text{mV}$. The red symbols show the measured position of the cell in the image sequence versus time, the blue curve shows the obtained regression for the last two driving periods that are shown. (b) Distribution of the resultant frequency of the measurements at an input voltage of $\Delta U_{\text{in}} = 1400\,\text{mV}$. N is the number of fits with a resultant frequency in the corresponding frequency interval. The green bars correspond to fits with a resultant frequency $f \in [99.5\,\text{Hz}, 100.5\,\text{Hz}]$. The resultant amplitudes of these fits were included into the calculation of the mean. The red bars correspond to excluded fits.

Figure 3.5 shows a typical fit of one dataset with a sinusoidal regression. The plotted range exceeds the fitting range of the regression by one period, but the curve describes all data points very well. To obtain a value of the amplitude for the whole image sequence we calculated the arithmetic mean of all regressions, excluding data where the difference between the resultant frequency and 100 Hz exceeds 0.5 Hz. As an example, Fig. 3.5 shows the distribution of the resultant frequency for the dataset taken at an input voltage of $\Delta U_{\text{in}} = 1400\,\text{Hz}$.

(3) To convert the motion measured from the images into metric units, we measure the outer height of the cell in the image of the static cell, h_{im}, as well as the true height of the cell h_{t}. The ratio $h_{\text{t}}/h_{\text{im}} = 0.135(4)\,\text{mm px}^{-1}$ is the constant of proportionality between the resultant amplitudes and the true shaking amplitudes.

The error is dominated by the conversion of the height differences in images into true height differences. This yields a relative uncertainty of less than 5 %.

Results

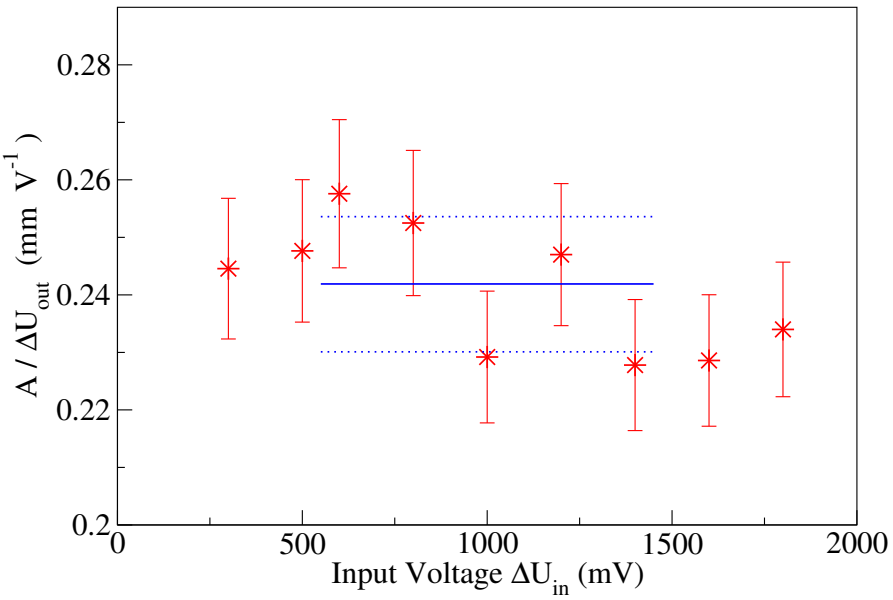

Figure 3.6: Ratio of the shaking amplitudes A and the peak-to-peak voltage difference of the accelerometer ΔU_{out} at different input voltages ΔU_{in}. The amplitude measurements and the accelerometer measurements were taken in two different experimental runs. The red stars show the measured data. The blue, continuous line shows the mean value and the blue, dotted lines correspond to the mean plus (minus) the standard deviation. The length of the lines indicate the range of the fitted data points. Both, the error of the individual measurements and the standard deviation are less than 5 %.

Figure 3.6 shows the ratio of the shaking amplitudes derived from image sequences A and the maximal voltage difference of the accelerometer ΔU_{out} for given input voltages from the signal generator. Note that the image sequences and the accelerometer measurements were obtained in two independent experimental runs.

The data fluctuate around a mean value. The deviations are caused by errors in the measurements of the driving amplitude as well as a variation of the true shaking amplitude between different experimental runs with the same driving parameters. The relative error in the amplitude measurements increases for low driving amplitudes. In contrast, we have observed that the shaker behaves less reproducibly at high driving amplitudes.[1] Therefore we calculate the mean and the

[1] If driven close to the limit, the shaker heats up. This leads to a small decrease of the shaking amplitude at constant ΔU_{in} with increasing experimental time.

standard deviation only for data ranging within $600\,\mathrm{mV} \leq \Delta U_{\mathrm{in}} \leq 1400\,\mathrm{mV}$. The standard deviation gives an estimate of the statistical error of the measurements and is approximately 4 %. It is in the same order of magnitude as the estimated experimental uncertainty of the individual measurements.

3.3 Result: Calibration Curve

Figure 3.7 shows the calibration curve obtained for the small cell C_2 and the large cell C_1 at driving frequency $f = 100\,\mathrm{Hz}$. The red symbols mark the points at which the acceleration was measured with the accelerometer. In both cases the data points do not follow a perfect linear curve. To convert intermediate values of ΔU_{in}, we use the `spline`-function provided by matlab - a cubic spline data interpolation - if $\Delta U_{\mathrm{in}}^{\mathrm{min}} \leq \Delta U_{\mathrm{in}} \leq \Delta U_{\mathrm{in}}^{\mathrm{max}}$. If ΔU_{in} exceeds this range, we interpolate linearly using the two closest data points. The interpolation is shown in Fig. 3.7.

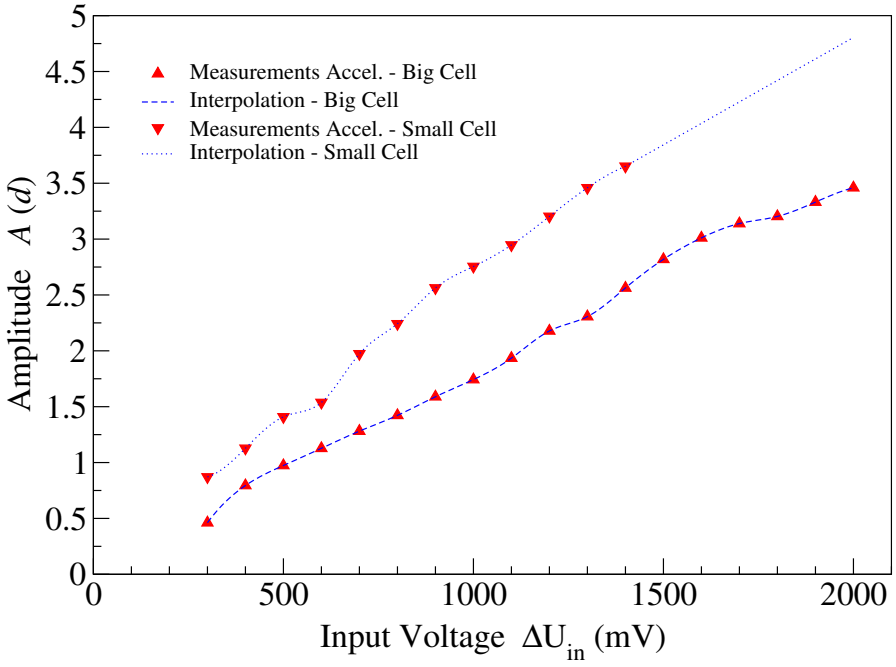

Figure 3.7: Calibration curve of the small cell C_2 and the large cell C_1 at driving frequency $f = 100\,\mathrm{Hz}$. The red symbols mark points at which the acceleration was measured with the accelerometer. The blue curves show the interpolation.

Most of the experiments were carried out at a driving frequency $f = 100\,\mathrm{Hz}$, but some of the measurements were carried out at another driving frequency. For driving frequencies $\tilde{f} \neq f = 100\,\mathrm{Hz}$ the curves need to be modified: For a fixed mass and input voltage the peak acceleration $\Gamma = d^2z/dt^2$ is frequency-independent. Thus Eq. (3.1) yields the relation

$$\frac{\tilde{A}}{A} = \frac{f^2}{\tilde{f}^2} \; ;$$

here A, and $\tilde{A}$ denote the corresponding shaking amplitudes.

The calibration process introduces a systematic error in the amplitude measurements. For the large cell C_1 and the small cell C_2 the error is dominated by the conversion of the accelerometer measurements into metric units and is less than $5\,\%$. For the large cell C_3, the error is more difficult to quantify, it is dominated by the additional intermediate step of comparing the input voltage differences of the instabilities in the large cell C_3 with those for measurements in the small cell C_2. We estimate the error to be less than $10\,\%$ by using the standard deviation of these measurements.

Chapter 4

Liquid-Gas-Like Phase Separation

At low filling fractions the system can separate into a dense, cold (liquid-like) and a dilute, hot (gas-like) phase. The phenomenon was closely studied [9, 12]: The separation is spinodal driven and emerges from a resonant motion of each particle in the gas-like phase leading to an excess in the granular temperature of the dilute phase. The amplitude at which phase separation occurs is independent of the driving frequency. The coarsening dynamics of the separation are described by the Cahn-Hilliard equation [67], also called model B in the Hohenberg-Halperin classification of dynamic critical phenomena [68]. Model B describes diffusive dynamics of systems minimising interfacial energy with a conserved order parameter. For a classical, molecular fluid the typical length scale l grows with time according to a power-law with a scaling exponent $\alpha = 1/3$ such that $l(t) \sim t^{\alpha}$. For the granular system, the scaling was reproduced experimentally and in simulations [12].

To familiarise myself with the apparatus we tried to reproduce parts of the work. In the following we discuss briefly our measurements and observations.

Measurements and Observations

The transient behaviour of the phase separation depends on the protocol used, while the steady-state is history-independent. If we jump instantaneously from an amplitude $A = 0$ up to an amplitude where the system phase separates and let the system evolve without changing the driving parameters until it stabilises,

we observe the following dynamics: At early times small droplets of the gas phase emerge throughout the whole cell. The pattern coarsens as the droplets push liquid areas between them aside and form larger domains of the dilute phase. These domains appear to minimise the interface by forming circular structures. For late times, smaller droplets evaporate and only large domains remain. A sequence of images of the coarsening dynamics is shown in Fig. 4.1. Similar dynamics were reported by Clewett *et al.* [12].

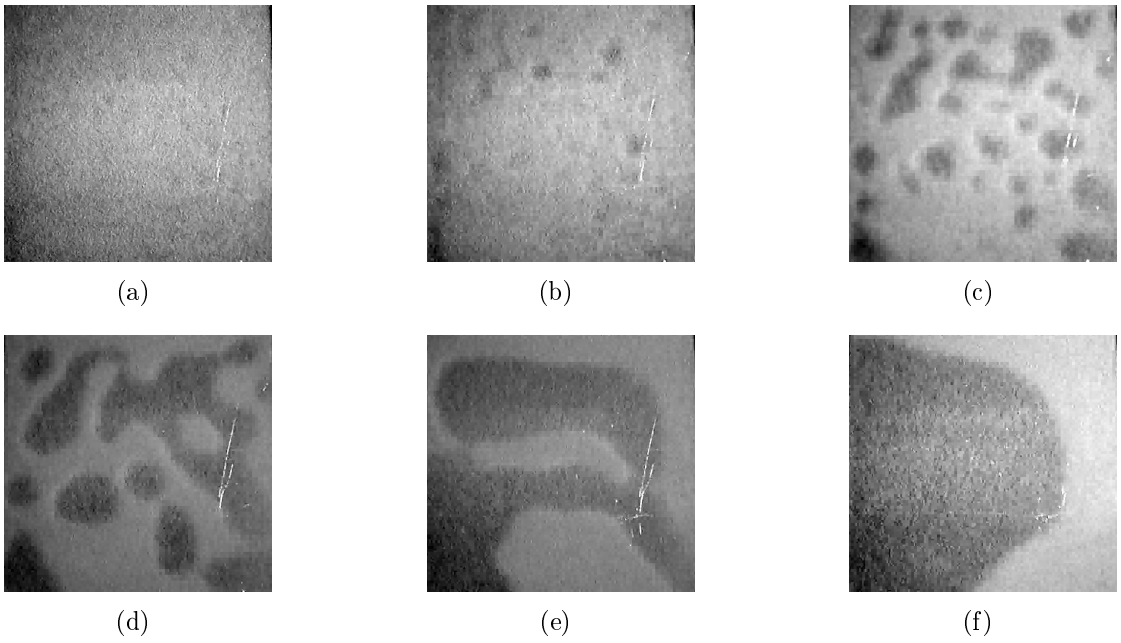

Figure 4.1: Sequence of photographs showing the time-evolution of the spinodal decomposition in the coexistence region following an instantaneous jump from $A = 0$ up to $A \approx 2.5d$. The mean volume filling fraction is $\phi = 5\,\%$, the driving frequency is kept constant at $f = 60\,\mathrm{Hz}$. The measurements were taken in the large cell C_3. The photographs were converted to greyscale. The boundaries of the pictures correspond to the boundaries of the cell. In (a) the system is homogeneous. Gradients in the intensity result from inhomogeneous lighting and reflections. The photograph was taken directly after the jump, $t = 0$. Images (b) - (f) were taken after the system was shaken for $t \approx 0.1\,\mathrm{s}$ (b), $t \approx 1\,\mathrm{s}$ (c), $t \approx 3\,\mathrm{s}$ (d), $t \approx 5\,\mathrm{s}$ (e) and $t \approx 8\,\mathrm{s}$ (f). The dark domains are the dilute, hot (gas-like) phase. The light area is the dense, cold (liquid-like) phase. Scratches in the bottom plate cause bright light reflections.

If the amplitude is not kept constant but increased slowly, we can explore the steady states for different amplitudes. At low amplitudes the system begins

in an approximately homogeneous state. At a critical amplitude a dilute bubble nucleates spontaneously and develops a circular shape. The bubble grows until its radius exceeds the dimensions of the cell, when the amplitude is increased further. At a second, higher, critical threshold the bubble completely fills the cell and the system is homogeneous again.

Phase Diagram

We measured the phase diagram in the large cell C_3 at a fixed driving frequency $f = 60\,\mathrm{Hz}$.

Experimental Procedure

During an individual experimental run, only the driving amplitude was changed, while other parameters were kept constant. For a fixed frequency $f = 60\,\mathrm{Hz}$ and a fixed filling fraction we measured the lowest and highest amplitude at which the system exhibits phase coexistence. We refer to these amplitudes as $A_{\mathrm{min}}(\phi)$ and $A_{\mathrm{max}}(\phi)$ respectively. It is important to note that the phase transition shows hysteresis. The data reported here were measured only for increasing amplitude. Starting with a homogeneous distribution of the particles in the whole cell (see section 2.3), we turned up the maximal input voltage difference in steps of $\delta U_{\mathrm{in}} = 10\,\mathrm{mV}$. This is the limit of the precision and gives an error of $\delta A \approx 0.06\,d$ in our measurements.

After each step, the system was allowed to relax to a steady state, before we took a photograph and analysed it as described in Sect. 2.2. The phases can be distinguished by the colour or greyscale intensity in the photograph. We determined whether a system is phase-separated by visually inspecting the manipulated images. The input voltage difference ΔU_{in} was converted into amplitudes as described in Sect. 3. This introduces a systematic error of less than 10 % in the measurements.

Results

The phase diagram is shown in Fig. 4.2. The symbol size exceeds the size of the error-bars.

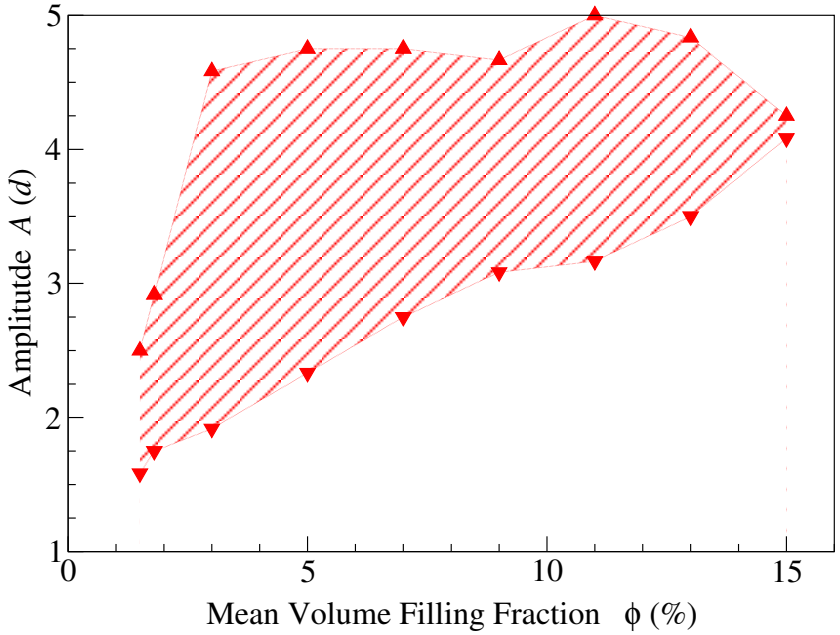

Figure 4.2: Phase diagram of the liquid-gas phase separation for constant driving frequency $f = 60\,\mathrm{Hz}$. ϕ denotes the mean volume filling fraction and A the driving amplitude measured in particle diameters d. The upward (downward) triangles mark the measured lowest (highest) amplitude of phase coexistence, $A_{\mathrm{min}}(\phi)$ ($A_{\mathrm{max}}(\phi)$). The shaded area shows the region of phase coexistence. The size of the triangles exceeds the size of the error-bars. All measurements were taken by increasing the driving amplitude in steps of $\Delta A = 0.06\,d$.

For high filling fractions, $\phi > 16\,\%$, no phase separation could be observed. We were unable to validate data for very low filling fractions, $\phi < 1.3\,\%$, for the following reasons: the size of the dense phase is so small that it becomes indistinguishable from tiny regions of higher density that are induced by a not perfectly level cell or because the steel base is slightly uneven. Additionally, the contrast of the bronze particles versus the light grey steel base is very low, so that variations of the local filling fraction are barely visible for small ϕ.

The shape of the locus $A_{\mathrm{min}}(\phi)$ is approximately linear. The locus $A_{\mathrm{max}}(\phi)$ rises steeply for $\phi \leq 2\,\%$, but flattens for higher ϕ. It saturates at $A \approx 5\,d$.

The shape of the phase diagram matches qualitatively with the one reported by Roeller *et al.* [9] for glass beads. The lowest and highest filling fraction of phase coexistence also agree quantitatively within small deviations with the data reported for the glass beads [9].

Chapter 5

Pattern Formation and Turbulence: Observations and Results

In the dense phase of the liquid-gas phase-separated system as well as for $\phi > 15\,\%$, we have observed different types of patterns. Each pattern consists of standing waves. As such, all patterns are inherently time-dependent, periodic. We call a pattern time-independent (or stationary in time) if the positions of the nodes and the maxima of the standing waves are stationary in time, that is if the pattern does not move in the horizontal plane. In contrast we call a pattern time-dependent if the nodes and maxima show a horizontal movement in the steady state.

At higher amplitudes the system descends into turbulent-like states: Waves sweep across the cell and a cell-filling large-scale circulation emerges when the amplitude is increased still further.

This chapter contains first a qualitative description of the different states and the development of the system with increasing driving amplitude for a fixed driving frequency and filling fraction. In the next part, we present the phase diagram obtained for a fixed frequency of $f = 100\,\mathrm{Hz}$ mapping out the stability regions of the different states in terms of the filling fraction and the driving amplitude. The frequency dependence of the different states is yet to be analysed in detail, but we present preliminary measurements of the frequency dependence of the lowest and highest amplitudes of the turbulent, wave-like state.

In the last part of this chapter we characterise the different states quanti-

tatively by measuring the topography spectra and frequency spectra for a fixed driving frequency of $f = 100\,\mathrm{Hz}$ and a fixed filling fraction of $\phi = 34\,\%$. Most experiments were carried out at $f = 100\,\mathrm{Hz}$, because the system is more sensitive to levelling at lower frequencies and the shaking acceleration approaches the limit of the electromagnetic shaker at higher frequencies.

5.1 Overview of the Different States

Figure 5.1 shows the pattern formation in the cell for steadily increasing driving amplitudes from $0.7\,d$ up to $2.5\,d$ at a fixed driving frequency of $f = 100\,\mathrm{Hz}$ and a volume filling fraction of $\phi = 32.5\,\%$.

At high driving frequencies the human eye cannot resolve the oscillation of the standing wave correctly, but perceives only the boundaries between countermoving regions. The effect can be visualized by changing the exposure time of photographs: If the exposure time exceeds the oscillation period, the boundaries show up as dark shadows; if the exposure time is small compared to one period of oscillation, the areas of different heights are resolved. Particles close to the top plate show up brighter than particles close to the bottom plate.

We have not observed a qualitative change in the different states upon changing the driving frequency or filling fraction. A typical development of the system with increasing driving amplitude is described below. In each case the new instability typically coexists with the previous state for a short range of amplitudes.

At the lowest amplitude, $A = 0.7\,d$, Fig. 5.1 (a), the particles are distributed homogeneously in the cell. If the amplitude is increased above a critical threshold, then the homogeneous surface becomes unstable and the system develops a stripe-like pattern. The pattern, shown in Fig. 5.1 (b) ($A = 1.2\,d$), is time-independent. We refer to this pattern as “low frequency stable stripes” (LFSS).

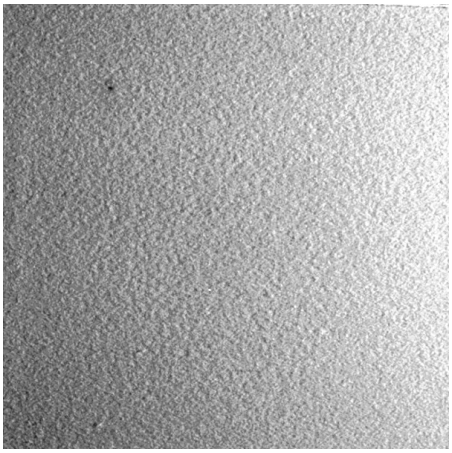

(a) homogeneous
$A \approx 0.7\,d$

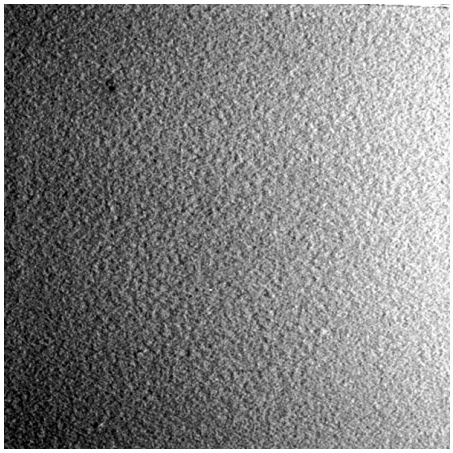

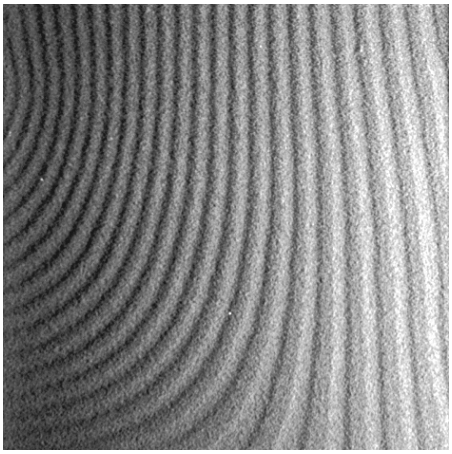

(b) LFSS
$A \approx 1.2\,d$

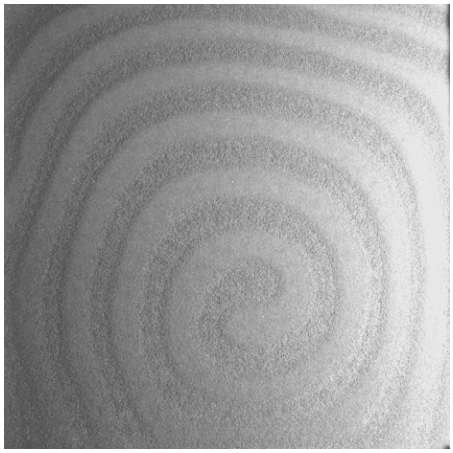

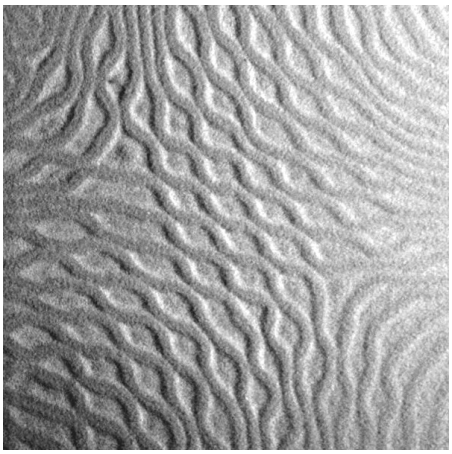

(c) LFSC
$A \approx 1.7\,d$

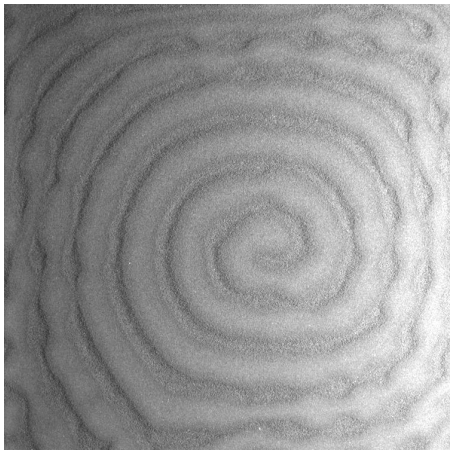

Patterns observed in the cell: homogeneous; low frequency stable stripes (LFSSS); low frequency stable crossrolls (LFSC). See page 41.

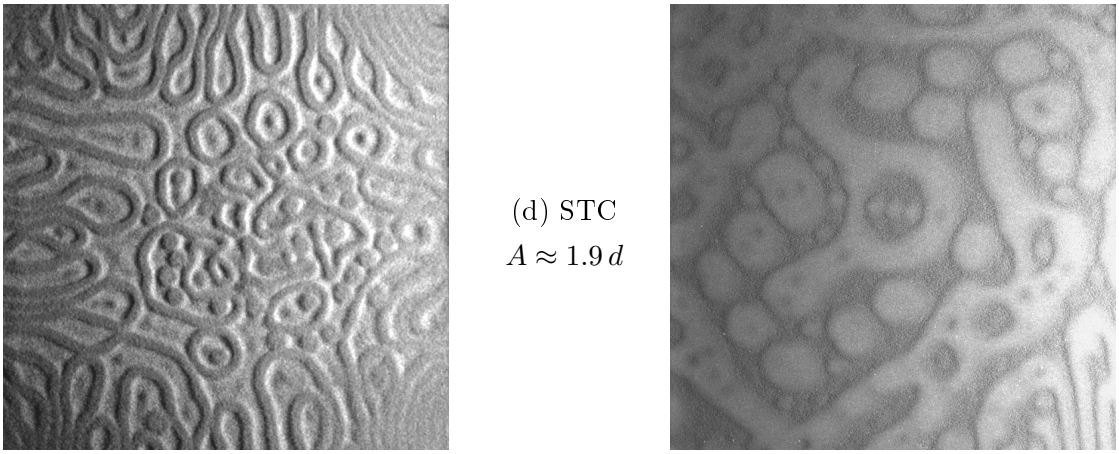

(d) STC
$A \approx 1.9\,d$

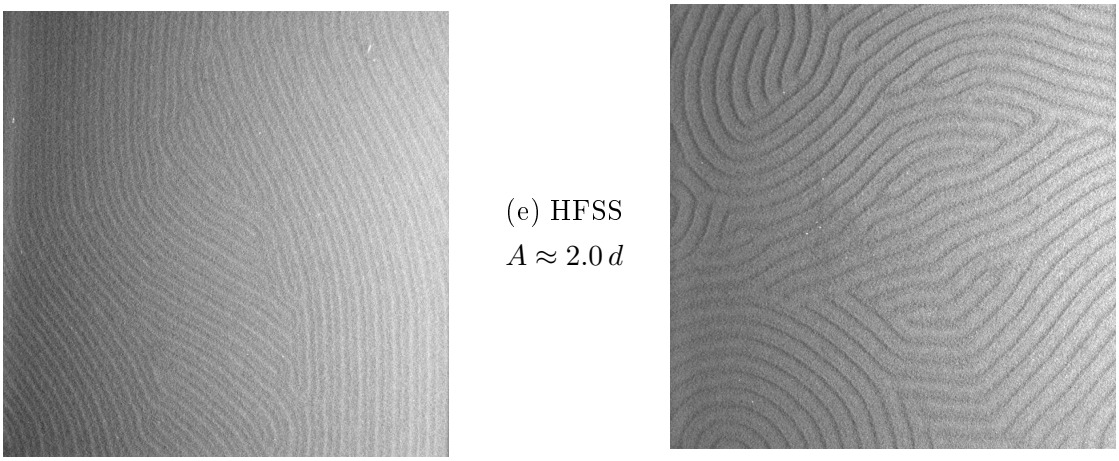

(e) HFSS
$A \approx 2.0\,d$

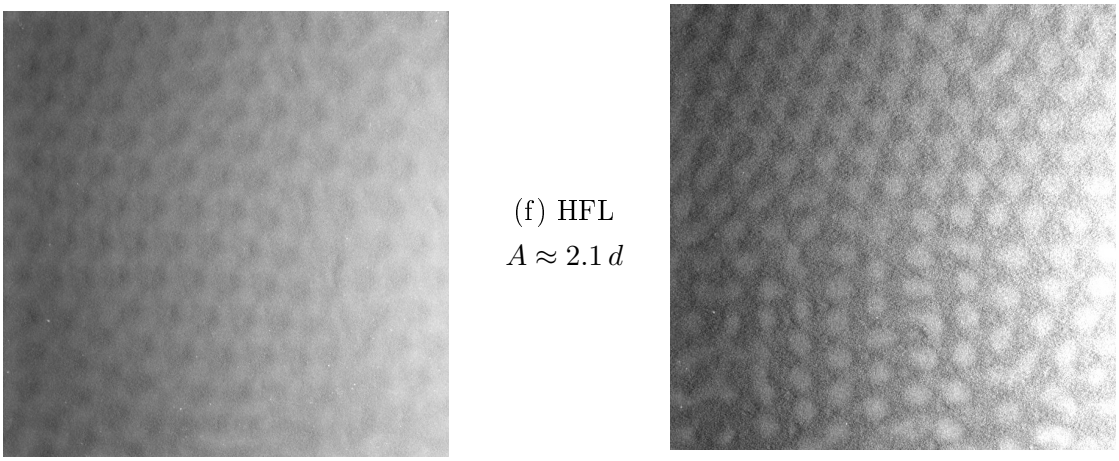

(f) HFL
$A \approx 2.1\,d$

Patterns observed in the cell: spatiotemporal chaos (STC); high frequency stable stripes (HFSS); high frequency lattice (HFL). See page 41.

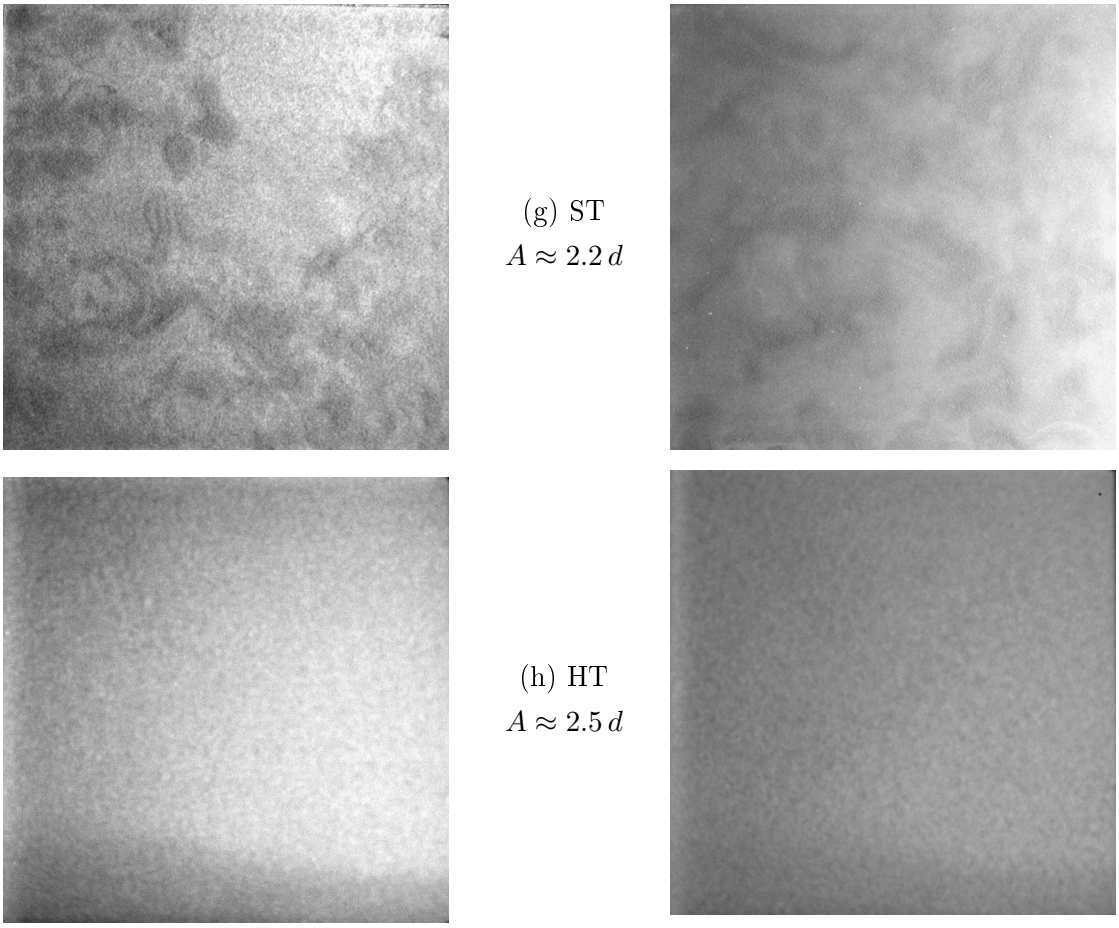

Turbulent states observed in the cell: soft turbulence (ST); hard turbulence (HT).

Figure 5.1: Sequence of images of the pattern formation in the cell for steadily increasing driving amplitudes from $A = 0.7\,d$ (a) up to $A = 2.5\,d$ (h). The mean volume filling fraction $\phi = 32.5\,\%$ and the driving frequency $f = 100\,\mathrm{Hz}$ were kept constant. The images were cropped to the boundaries of the large cell C_1 and converted to greyscale. The photographs at the left hand side were taken with long exposure time $T = 20\,\mathrm{ms}$ (2 cycles) the photographs at the right side with short exposure time $T = 2\,\mathrm{ms}$ (1/5 of a cycle). The pictures were taken in different experimental runs: Panels (b), (c) and (h) show different structures of the same state. A description of the development of the pattern can be found in Sect. 5.1.

In general, the shape of the pattern depends on the protocol used. In the steady state the pattern consists of parallel stripes or a cell-filling spiral. The stripes tend to align perpendicular to the side-walls and could be observed in all cells. Spiral patterns emerged only in the large cell C_1, we attribute this

to the rounded corners of that cell. If, starting from a stable flat surface, the driving amplitude is increased slowly above the instability threshold, only stripes emerge. If instead the critical amplitude is crossed by abruptly increasing the driving amplitude, patterns of circles, spirals (only in cells with rounded corners) or striped regions which contain many defects appear. The dynamics are slow, but after a long time (approximately 10 min) the circles annihilate into stripes and defects migrate outward and disappear at the boundaries of the cell. Figure 5.2 shows the different structures of the LFSS. The ordering dynamics are shown in a video in the supplementary material (see Sect. A.2). Close to the critical amplitude the wavenumber of the low frequency stable stripes is $k/(2\pi) \approx (50\,d)^{-1}$, this is independent of the structure of the pattern. With increasing driving amplitude, the typical length scale of the pattern increases.

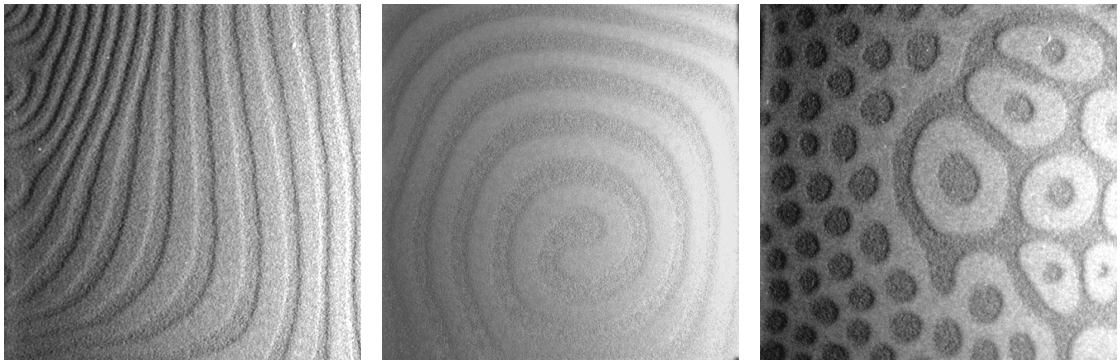

(a) Stripes (b) Spiral (c) Circles

Figure 5.2: Different structures of the low frequency stable stripes at driving frequency $f = 100\,\mathrm{Hz}$, driving amplitude $A \approx 1.2d$ and filling fraction $\phi = 32.5\,\%$ The stripes (a) and the spiral (b) show a steady-state pattern. The circles (c) are only an intermediate state and finally develop into a stripe or a spiral pattern. The photographs were taken with short exposure time $T = 2\,\mathrm{ms}$ and converted to greyscale. The edges of the image correspond to the boundaries of the large cell C_1.

Figure 5.1 (c) ($A = 1.7\,d$) shows the pattern after the system bifurcated again. Parallel stripes and spirals of the low frequency stable stripes develop into a pattern that looks very similar to the well-known cross-roll instability [18]. Circles of the LFSS develop an additional domain in the centre (see Fig. 5.3). This pattern is also time-independent. We refer to this state as "low frequency stable crossrolls" (LFSC).

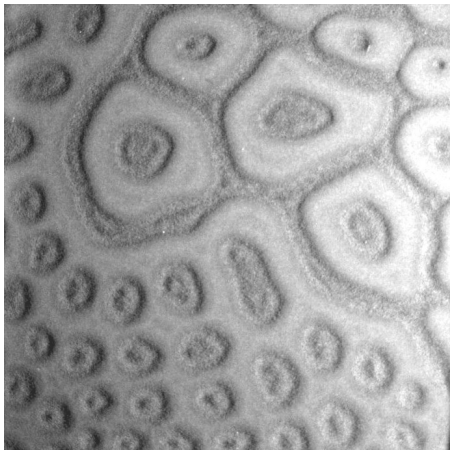

Figure 5.3: Picture of the low frequency stable crossrolls that can be observed upon slowly increasing the driving amplitude, if the low frequency stable stripes consisted of droplets. The bifurcation emerged as additional droplets in the circles. The photograph was taken with short exposure time $T = 2\,\mathrm{ms}$ and converted to greyscale. The edges of the image correspond to the boundaries of the large cell C_1.

As the driving amplitude increases further the stripes begin to shiver up to a point when the pattern changes its shape rapidly. The movement grows from the centre of the cell. Single snapshots of the time-dependent pattern is shown in Fig. 5.1 (d) ($A = 1.8\,d$). The images also show examples of short-lived circular structures which coexist with the stripes at this driving amplitude. The circles appear rapidly and either merge with a nearby stripe or disappear equally rapidly. We refer to this state as "spatiotemporal chaos" (STC).

The next bifurcation, Fig. 5.1 (e) ($A = 2.0\,d$), introduces high-wavenumber ($k/(2\pi) \approx (25\,d)^{-1}$) parallel stripes at the edge of the cell. The stripes grow until they fill the whole cell and tend to align perpendicular to the walls. The pattern is again time-independent. We refer to this state as "high frequency stable stripes" (HFSS). As for the LFSS the pattern can emerge with several defects that disappear if the system is allowed to relax. Only at very high filling fractions, $\phi \geq 45\,\%$, this pattern develops a time-dependence at higher driving amplitudes, such that the stripes move ("high frequency moving stripes" (HFMS)).

Figure 5.1 (f) ($A = 2.1\,d$) shows another time-dependent pattern. In contrast to the other states this state develops at the edge of the cell independently of the existing high-wavenumber stripes. Suddenly, the system exhibits a hexagonal lattice of valleys and peaks. The typical length scale of this lattice is larger than the typical length scale of the HFSS, but smaller than the length scale of the LFSS. We refer to this state as the "high frequency lattice" (HFL).

In the penultimate state, Fig. 5.1 (g) ($A = 2.2\,d$), remarkably pronounced waves

sweep across the cell. In the experiment the waves always emerge from the side walls. They are accompanied by a loud pulsing sound. The evolution of the patterns that exist at lower amplitudes is somewhat similar to those observed in RBC experiments of molecular fluids. In RBC, for very high temperature differences, the system reaches a turbulent state. This invites the question: are the waves observed here an example of turbulence in a granular system? In Sect. 5.4 we present evidence that this state is indeed turbulent. For now we refer to this state as "soft turbulence" (ST). Near the instability threshold the pattern of the previous state still underlies the waves. The patterns are gradually destroyed with increasing amplitude.

For very high amplitudes, $A \approx 2.5\,d$ a slow large-scale circulation (LSC) pushes the waves to the edges of the cell until only the circulation remains. Large-scale circulation can also be observed in two-dimensional turbulence and in the hard turbulent regime of Rayleigh-Bénard convection in molecular fluids [69, 70]. We call this state "hard turbulence" (HT), once again drawing the analogy with RBC experiments at very high temperature differences. In this state the cell looks homogeneous in photographs, Fig. 5.1 (h). In Fig. 5.4 and in a video in the supplementary material (see Sect. A.2) the flow is visualized with tracer particles. No preferred orientation of the flow could be observed. The speed of the circulation increases with driving amplitude until it eventually breaks up into smaller eddies. Ultimately the granular gas looks somewhat jelly-like.

The videos of the different states in the supplementary material (see Sect. A.2 show the dynamics of the system. The normal-speed videos illustrate the dynamics of defect annihilation in the LFSS- and the HFSS-state as well as the time-dependence of the STC. The videos taken with the high-speed camera show the frequency of the pattern with respect to the driving frequency.

Visualization and dynamics of the large-scale circulation

The flow usually forms one large, nearly cell-filling vortex, but sometimes two counterrotating eddies are observed. The orientation of the vortex varied upon every experimental run. We also observed, though very rarely, the cessation of a LSC and its restarting with the opposite orientation. The circulation does not

immediately set in when the driving amplitude is set to the target amplitude of the HT-state. The time required to establish the flow varies slightly upon every experimental run and increases significantly with increasing filling fraction.

To visualize the large-scale circulation, a few spherical, steel tracer particles of diameter $D = 2\,\mathrm{mm} = 10\,d$ were placed in the cell. Particles of the same size or smaller than the bronze particles would "disappear" in the bulk and could not be distinguished visually when the cell is shaken. The experiment was carried out in the small cell C_2 with a filling fraction of $\phi = 40\,\%$ at a driving frequency of $f = 100\,\mathrm{Hz}$ and an amplitude of $A = 4.25\,d$. Initially the tracer particles were distributed homogeneously in the cell and the amplitude was increased rapidly to the target amplitude of the HT-state to avoid segregation.[1] Nevertheless only one steel particle caught up the mean flow whereas the others clustered in one corner of the cell. In photographs of very long exposure time, $T \geq 0.5\,\mathrm{s}$, the tracer particle is blurred out by noise such that it cannot be distinguished. Instead we took a sequence of photographs with a time step of $\Delta t = 0.4\,\mathrm{s}$ and marked the position of the particle in each image. Figure 5.4 shows the superposition of the images. The speed of the tracer particle does not necessarily equal the speed of the bulk flow, because the tracer particle differs in mass, size and coefficient of restitution from the bronze particles.

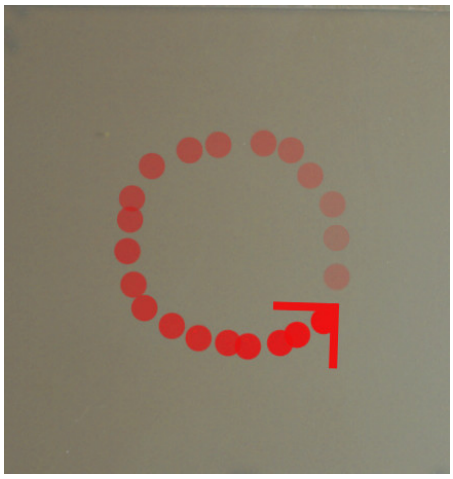

Figure 5.4: Visualization of the large-scale circulation using a tracer particle. The image shows the superposition of a sequence of photographs of a large-scale circulation in the small cell C_2. The photographs were taken with a time-step of $\Delta t = 0.4\,\mathrm{s}$ and the position of the tracer particle was marked with a big, red circle in every picture. The images were superimposed such that the opacity of the circle increases with time. The arrow indicates the direction of the flow. The experiment was carried out in the small cell C_2 with a filling fraction of $\phi = 40\,\%$ at a driving frequency of $f = 100\,\mathrm{Hz}$ and an amplitude of $A = 4.25\,d$.

[1] Molecular fluids usually mix when being stirred. In contrast a mixture of granular materials often unmixes when it is stirred, shaken or sheared [71]. A difference in particle size, shape, density or even surface roughness can cause segregation. For a detailed review see [71].

"Pre-Pattern"

At very low driving amplitudes, we have observed a labyrinthine pattern with a wavenumber of $k/(2\pi) \approx (10\,d)^{-1}$, that means that the typical length scale of this pattern is much smaller than the typical length scale of the patterns described above. An image of the pattern is shown in Fig. 5.5; the additional material contains a high-speed movie of the pattern illustrating, that this pattern oscillates at $f/2$, too. If the driving amplitude was increased slowly from $A = 0\,d$, the pattern usually emerges directly after the "fluidisation point", the driving amplitude at which the peak acceleration equals the gravitational acceleration, such that the particles leave the bottom plate. If the amplitude is increased further, the pattern usually disappeared below the instability threshold of the patterns described above. We did not study this pattern further.

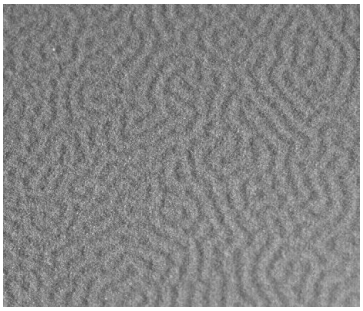

Figure 5.5: Photograph of the small "pre-pattern" observed at very low driving amplitudes $A \leq 1\,d$. The photograph shows one quarter of sthe large cell C_1 with filling fraction $\phi = 32.5\,\%$, driving frequency $f = 100\,\mathrm{Hz}$ and amplitude $A = 0.8\,d$. The image was taken with short exposure time $T = 2\,\mathrm{ms}$ and converted to greyscale.

5.2 Phase Diagram

We measure the phase diagram for a fixed driving frequency $f = 100\,\mathrm{Hz}$. The parameter space in which we map out the stability regions of the different states is spanned by the driving amplitude and the volume filling fraction. We obtain the phase diagram by identifying the onset amplitudes of the different states. All bifurcations show hysteretic behaviour. We measure the phase diagram only for slowly increasing driving amplitude.

We observe pattern formation and turbulence at filling fractions ranging between $\phi = 15\,\%$ and $\phi = 60\,\%$. No experiments were carried out at filling fractions $\phi > 60\,\%$. The amplitude of the different states ranges between $1\,d$ and $4.75\,d$.

Experimental Procedure

We mapped out the phase diagram by measuring the bifurcation points of the system, i.e. the amplitudes ("onset amplitude") at which the different phenomena appear first when the amplitude is increased slowly. Typically, the phenomena emerge locally in one region and fill the entire cell when the amplitude is increased slightly. A small range of coexistence of two different patterns can be observed even in a carefully levelled cell. We mark only the first appearance of a pattern. The filling fraction was increased up to $\phi = 60\,\%$ in steps of $2.5\,\%$. Measurements with filling fractions $\phi \leq 42.5\,\%$ were taken in the large cell C_3. For practical reasons we could not fill the large cell C_3 beyond $42.5\,\%$, therefore we continued the measurements using the small cell C_2. In order to compare the different systems, we repeated the measurements taken with the large cell C_3 at $\phi = 32.5\,\%$ in the small cell C_2.

To avoid experimental bias, the measurements were taken by two people. One turned up the amplitude slowly, the other watched the cell and identified the onset amplitude of the different states without looking at the amplitude display of the signal generator. The data were recorded in terms of the peak-to-peak voltage ("input voltage") of the signal generator. Great care was taken that the cell was level at each amplitude.

Data Analysis

The onset amplitudes recorded in terms of the input voltage ΔU_{in} need to be converted into driving amplitudes. In the following, the superscripts "3, 2" refer to the large cell C_3 and the small cell C_2 respectively. For measurements with the small cell C_2, ΔU_{in}^2 is converted into a driving amplitude as described in Sect. 3.

For the large cell C_3 we use the measurements at $\phi = 32.5\,\%$ that were taken in both systems. Figure 5.6 shows the ratio of the input voltages of the onset amplitudes $\Delta U_{\text{in}}^3/\Delta U_{\text{in}}^2$ (red symbols). The blue, continuous line shows the mean value $\beta = \langle \Delta U_{\text{in}}^3/\Delta U_{\text{in}}^2 \rangle$. The standard deviation of the sample σ_β is less than $10\,\%$. The range $[\beta + \sigma_\beta,\ \beta - \sigma_\beta]$ is indicated by the blue, dotted lines. In this way we convert the input voltages of measurements taken with the large cell C_3 into corresponding input voltages in the small cell C_2 by a multiplication with

$\langle \Delta U_{\mathrm{in}}^3 / \Delta U_{\mathrm{in}}^2 \rangle$ and proceed as described in Sect. 3.

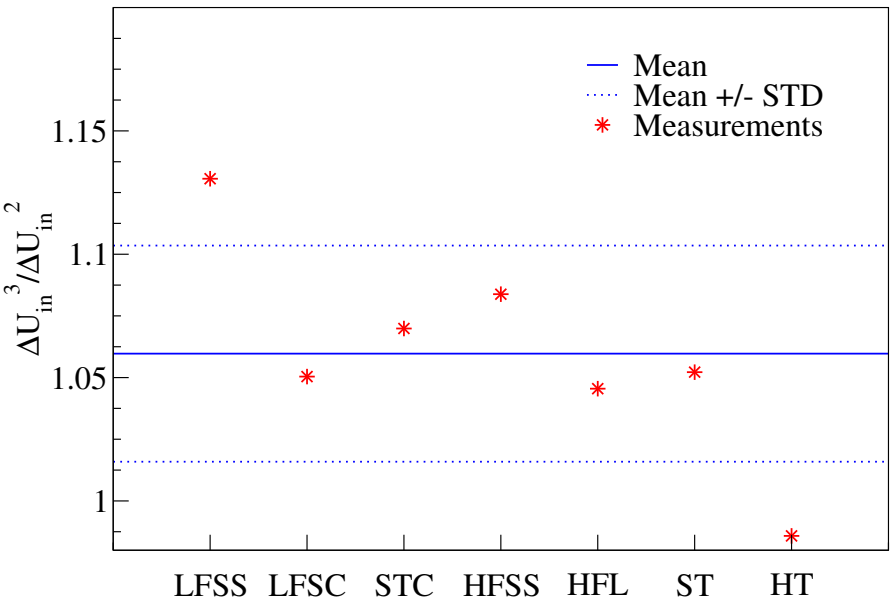

Figure 5.6: Ratio of the input voltage differences $\Delta U_{\mathrm{in}}^3 / \Delta U_{\mathrm{in}}^2$ at which the different states appear for experiments taken with the large cell C_3 and the small cell C_2. ΔU_{in}^3 is the required input voltage of the signal generator for experiments with the large cell C_3 and ΔU_{in}^2 refers to experiments with the small cell C_2. The abbreviations refer to the different states as introduced in Sect. 5.1. The red symbols show the measured data. The blue, continuous line shows the calculated mean value; the blue, dotted lines show the mean plus/minus the standard deviation respectively. The standard deviation is less than 10 %, the size of the symbols exceeds the size of the error bars of the experimental precision of an individual measurement.

Results

Figure 5.7 shows the measured onset amplitudes for the different states that we observe. For the sake of clarity the figure does not contain error-bars. The experimental precision of an individual measurement is limited by the step size of the signal generator, it is less than 1 %. The corresponding error-bar is smaller than the symbol-size. The systematic error caused by the calibration process was estimated to be less than 5 % for measurements in the small cell C_2 ($\phi > 45\,\%$) and less than 10 % for the measurements in the large cell C_3 . In each case the new instability typically coexists with the previous state for a short time.

Pattern formation was present for filling fractions ranging between 15 % up to the highest realised filling fraction $\phi = 60\,\%$. At low filling fractions, $\phi \leq 15\,\%$, neither pattern formation nor turbulent states could be observed. At filling fractions in the range of $1\,\% \leq \phi \leq 16\,\%$, the system separates into a dilute, gas-like and a dense, liquid-like phase (see Chap. 4). Pattern formation can be observed only in the liquid phase, where the local filling fraction ϕ_l exceeds the

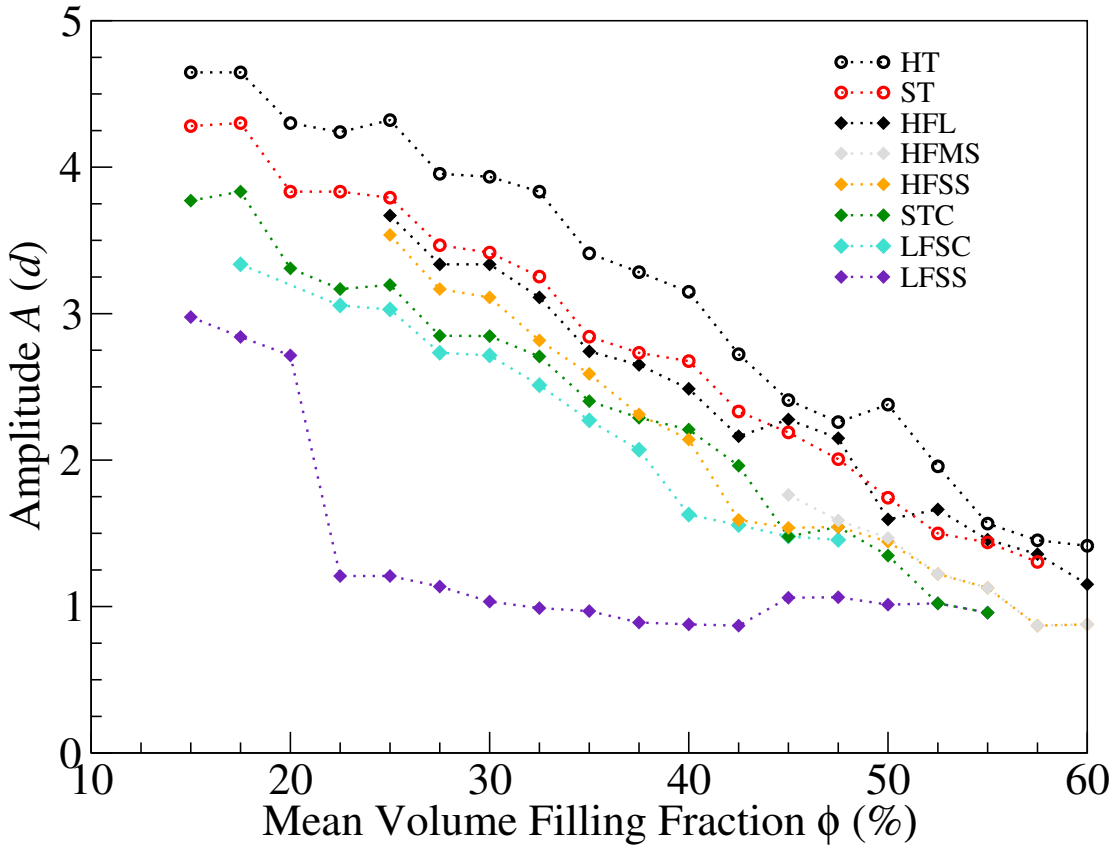

Figure 5.7: Phase diagram at fixed driving frequency $f = 100\,\mathrm{Hz}$: The data points mark the bifurcation points of the system, that is the onset amplitudes of the different states. The diamonds show the instability threshold of the different patterns and the circular symbols mark the transition to the turbulent states. Above $\phi = 60\,\%$ no experiments were carried out, below $\phi = 15\,\%$ neither pattern formation nor turbulent states can be observed. The size of the symbols exceeds the size of the error bars of the experimental precision. The first instability decreases abruptly at $\phi = 20\,\%$ and fluctuates around a mean value for higher filling fractions. The amplitudes of instabilities of higher order decreases within small deviations monotonically with increasing filling fraction. The dashed lines are guides for the eye.

mean filling fraction ϕ.

The onset amplitude of the low frequency stable stripes, the first bifurcation, drops significantly at $\phi = 20\,\%$. The jump coincides approximately with the disappearance of the liquid-gas phase separation. At higher filling fractions, $\phi > 20\,\%$, the onset amplitude of the low frequency stable stripes is approximately filling fraction-independent and fluctuates around a constant value $A_{\text{first}} \approx 1.25\,\text{d}$; it is slightly higher for measurements taken in the small cell C_2 ($\phi \geq 45\,\%$) than for measurements in the large cell C_3 . In contrast the amplitudes of all other instabilities decrease within small deviations monotonically with increasing filling fraction.

The system shows the high frequency states (HFSS and HFL) only if the filling fractions exceeds 25 %. The transition from the high frequency stable stripes into a time-dependent pattern of the same typical length scale could not be observed at filling fractions $\phi \leq 45\,\%$. In turn, the low frequency states disappear at very high filling fractions. We note that, at low filling fractions the first temporal instability (STC) precedes the high frequency stripes. However, for very large filling fractions the high frequency stripes occur at a lower amplitude than the first temporal instability.

With increasing filling fraction the visibility of the patterns is reduced. It is possible that above 52.5 % the measured amplitudes of the high frequency stable stripes and the high frequency moving stripes should actually correspond to the low frequency stable stripes and spatiotemporal chaos respectively.

Discussion

The measurements taken in the large cell C_3 are concatenated with the measurements in the small cell C_2 between $\phi = 42.5\,\%$ and $\phi = 45\,\%$. The transition shows up clearly in the phase diagram. As for the measurements at $\phi = 32.5\,\%$ that were taken in both systems the onset point of the low frequency stripes in the small cell C_2 is higher than in the large cell C_3. In both cases the data vary by less than 10 %. The deviations might be caused by a flexing of the large cell C_3 at high accelerations.

The transition to the small cell C_2 coincides with the appearance of the high

frequency moving stripes in the phase space. We assume, that the change of system does not cause the appearance of this state, because the behaviour in the large cell C_3 at lower filling fractions can be reproduced in the small cell C_2. Qualitatively the small cell C_2 shows the same patterned and turbulent states and quantitatively the ratio $\Delta U_{\mathrm{in}}^3/\Delta U_{\mathrm{in}}^2$ of the onset points varies less than 10 %.

Except for the onset point of the low frequency stable stripes, the onset points of all other states decrease with increasing filling fraction. As a first approximation, the decrease seems linear. The slope of the curves varies for the different instabilities and seems to increase with increasing order of the instabilities. The data differ from a perfect linear curve. As an example we illustrate the discrepancy for the amplitudes of the transition to the soft turbulent state. This instability threshold decreases from $A \approx 4.25\,\mathrm{d}$ at $\phi = 15\,\%$ to $A \approx 1.7\,\mathrm{d}$ at $\phi = 57.5\,\%$.

A detailed understanding of the filling fraction dependence of the onset amplitude of the instabilities would be an important step towards a theoretical modelling of the instabilities and dynamics of this system.

5.3 Frequency Dependence

We observed the patterned and turbulent states at driving frequencies ranging between 50 Hz and 130 Hz. For very low driving frequencies $f < 50\,\mathrm{Hz}$ the cell could not be levelled adequately.[2] No experiments were carried out at high driving frequencies $f > 130\,\mathrm{Hz}$, because the shaking acceleration, $\Gamma \propto f^2$, approaches the limit of the electromagnetic shaker at these frequencies and we did not want to damage the shaker.

A detailed study of the frequency dependence of the different states is yet to be carried out, but we have measured the lowest and highest amplitudes (or equivalently accelerations) of the soft turbulent state for a fixed filling fraction $\phi = 40\,\%$ for $50\,\mathrm{Hz} < f < 130\,\mathrm{Hz}$. For $f > 100\,\mathrm{Hz}$ only the lowest amplitude of the soft turbulent state was measured, because at these frequencies the acceleration at the transition to the hard turbulent state was beyond the limit of the electromagnetic shaker in this frequency range.

[2] The cell is less sensitive to levelling for higher driving accelerations, because gravity becomes less important.

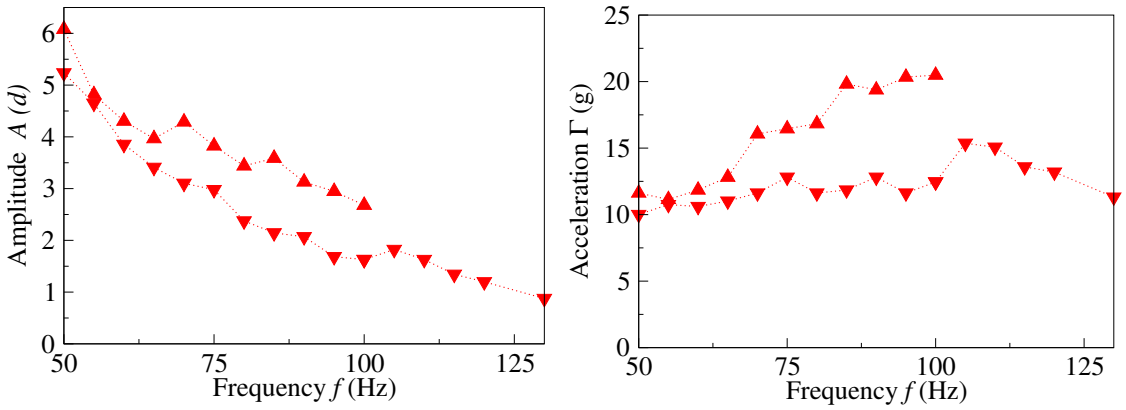

(a) (b)

Figure 5.8: Frequency dependence of the turbulent state for a fixed filling fraction of 40 %. Panel (a) shows the lowest and highest amplitude A/d of the soft turbulent state and panel (b) the corresponding accelerations Γ/g; here g is the gravitational acceleration.

The experiments were carried out in the large cell C_3. The experimental procedure for an individual measurement is the same as the procedure for the measurements of the phase diagram. A precise description is given in Sect. 5.2. The data were converted into amplitudes and accelerations as described in Sect. 3 and 5.2.

In Fig. 5.8 (a) the onset amplitudes, A, are plotted against the driving frequency, f. Figure 5.8 (b) shows the corresponding onset accelerations $\Gamma = A(2\pi f)^2$. As for the previous measurements the experimental precision is given by the step size of the signal generator. The size of the corresponding error-bars is less than the size of the symbols. The systematic error due to the calibration is less than 10 %, because the measurements were taken in the large cell C_3. Within small deviations the lowest and the highest amplitude of the soft turbulent state decrease monotonically with increasing driving frequency. At low frequencies, $f < 70\,\mathrm{Hz}$, both curves fall steeply. The slope decreases a little at higher frequencies. In contrast the curves of the highest and lowest acceleration Γ raise at low frequencies and seem to saturate for higher frequencies $f \geq 90\,\mathrm{Hz}$ at accelerations of $\Gamma \approx 12\,g$ and $\Gamma \approx 20\,g$ respectively; g is the gravitational acceleration.

Discussion As discussed in Chap. 6 a saturation of the onset amplitudes would suggest that gravity becomes negligible, whereas a saturation of the acceleration implies, that gravity, though one order of magnitude smaller than the peak shaking acceleration Γ still plays a crucial role. The measured data might be influenced significantly by a frequency-dependence in the shape of the driving wave function. The calibration performed with the accelerometer shows that the sinusoidal driving is affected by noise. The level of noise depends on the amplitude and the frequency. The data collected thus far does not allow for a clear interpretation. In order to ascertain the frequency dependence of the patterned and turbulent states closely, it would be necessary to reduce the noise in the shape of the driving.

5.4 Spatial Power Spectra of the Topography

In this section we characterise the spatial structure of the states for a fixed filling fraction $\phi = 34\,\%$ and a fixed driving frequency $f = 100\,\mathrm{Hz}$ quantitatively. The experiments were carried out in the large cell C_1. Therefore, we measure the spatial power spectra of the images for the different states. The brightness in the image is correlated to the topography, because particles sticking to the top glass plate show up brighter than particles at the bottom of the cell. Consequently we assume that we obtain the power spectrum of the topography $S_s(k)$ from the images. We exclude the hard turbulent state from this analysis, because the system appears homogeneous in photographs.

Experimental Procedure

During all experiments, the driving frequency $f = 100\,\mathrm{Hz}$ and the filling fraction $\phi = 34\,\%$ were kept constant. Except for the low frequency stable stripes, the amplitude dependence of the typical length scale of the pattern is within the range of our experimental precision, so that we present only one dataset at one driving amplitude ("target amplitude") for each of these states. The target amplitudes were chosen such that the pattern fills the whole cell: $2.5\,d$ (LFSC), $2.7\,d$ (STC), 2.8 (HFSS), $2.9\,d$ (HFL) and $3.3\,d$ (ST). The pattern of the low frequency stable stripes coarsens significantly with increasing driving amplitude so that we mea-

sure the spectra for seven different target amplitudes $1.2\,d$, 2.3, $1.5\,d$, $1.6\,d$, 1.8, $2.1\,d$ and $2.2\,d$. The amplitudes cover nearly the whole amplitude range from the onset amplitude of the low frequency stable stripes up to the transition to the low frequency stable crossrolls.

The spectra are obtained from images recorded with the `Olympus Digital E-500` Camera at a short exposure time $T = 2\,\mathrm{ms}$. For each dataset (each target amplitude) 10 sets of 10 images at the target amplitude were taken. Each set of images was obtained in an individual experimental run to ensure some statistical accuracy.

Protocol

At the beginning of each experimental run the particles were distributed homogeneously throughout the cell. The target amplitude was approached by decreasing the driving amplitude quickly from a value where the system is in the soft turbulent state, and as such, well mixed. At the target amplitude the system was allowed to relax until the typical length scale did not change in time. The images were recorded at different phases of the shaking, because the camera was controlled manually.

Additionally, one image sequence of each state was taken with the high-speed `PCO.1200s` camera. The frame rate of the high-speed camera was fixed at the maximum frame rate of $500\,\mathrm{s}^{-1}$, so that every fifth image of a set corresponds to the same phase of the shaking.

Data Analysis

The images are manipulated as described in Sect. 2. We calculate the discrete, two-dimensional Fourier transform of the manipulated images using the `fft2`-function provided by `matlab`. We consider the spatial Fourier transform of the patterns with wave vector $\vec{k} = (k_x,\, k_y)^t$. For every set the average of the Fourier transforms of all images at the same target amplitude appears rotationally symmetric.[3] This allows us to perform a radial average over all directions. Thus, we reduce the

[3]Note that only the average of the Fourier transform of all images and not the Fourier transform of one individual image is rotationally symmetric.

complexity and characterise the spectrum of an image in terms of the single scalar value $k = \sqrt{k_x^2 + k_y^2}$. We ignore the DC-term $k = 0$ as it only represents the mean brightness of the images.

The lighting of the cell does not only create an intensity gradient at the length scale of the cell, but can also cast small-scale shadows. The shadows are not removed by the previous image manipulation and appear as additional peaks in the spectra. The presence of the shadows in the images depends on the phase of shaking when the image was taken. We identify the peaks corresponding to shadows as described below and exclude the images, where these peaks are dominant in the spectrum We average the power spectra of the remaining images of each target amplitude.

To identify the artificial peaks, we use the sequence of images taken with the high-speed camera at constant frame rate. For these images we carry out the data analysis as described before, but finally average only over the spectra taken at the same phase of shaking. Some peaks appear in the averaged spectra independent of the phase of shaking, whereas other peaks disappear entirely at a particular phase. As an example, Fig. 5.9 shows the averaged spectra at different phases for the high frequency stable stripes. The peak at the main maximum appears in each spectrum, whereas minor maxima disappear entirely at one phase. The length-scale that corresponds to the minor maxima is in the range of the width of the shadows, so that we identify these peaks with the shadows.

Results

Figure 5.10 shows the datasets corresponding to the first bifurcation into the low frequency stable stripes. All spectra show one clear single peak. At the lowest realised shaking amplitude $A = 1.2\,d$ the corresponding wavenumber is $k/(2\pi) = 0.72\,\mathrm{cm}^{-1}$, such that the corresponding typical length scale is $L = 1.39\,\mathrm{cm}$. With increasing shaking amplitude, the position of the peak decreases to lower k-values, which corresponds to an increase in the typical length scale. At the highest realised amplitude for the low frequency stable stripes, the spectrum peaks at $k/(2\pi) \approx 0.39\,\mathrm{cm}^{-1}$ such that the typical length scale is $L = 2.56\,\mathrm{cm}$.

The typical length scale does not increase linearly with the shaking ampli-

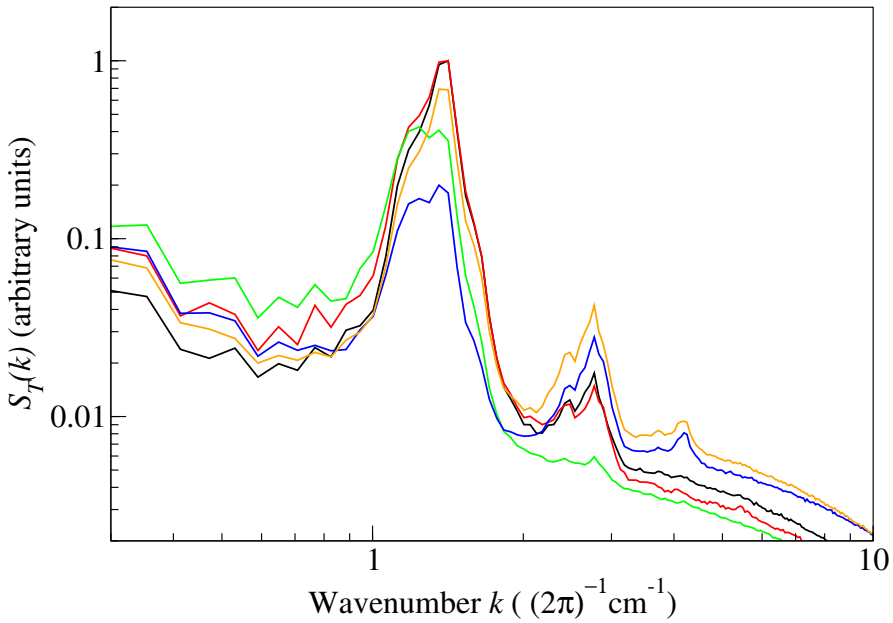

Figure 5.9: Dependence of the power spectrum of the topography on the shaking phase for the high frequency stable stripes. The different curves correspond to different phases of the shaking. The main maximum appears clearly in every dataset. The minor maxima disappear entirely at one particular phase of shaking.

tude, but raises steeply within a small range of low amplitudes and increases only marginally in a wide range of higher amplitudes. There was not time to complete a full analysis of the change in the length scale with driving amplitude.

Figure 5.11 shows the spectra obtained for the other states as well as the spectrum of the highest amplitude for the low frequency stable stripes. The spectrum of the low frequency stable crossrolls shows a peak at $k/(2\pi) \approx 0.5\,\mathrm{cm}^{-1}$ that is about the same wavenumber as the peak of the low frequency stable stripes. Additionally a minor peak at a higher wavenumber $k/(2\pi) \approx 1.06\,\mathrm{cm}^{-1}$ corresponding to an additional, clear, smaller typical length scale $L \approx 0.94\,\mathrm{cm}$ appears in the power spectrum. In the spectrum for the spatiotemporal chaos, the first two peaks reappear at slightly smaller wavenumbers and additionally a clear tertiary peak appears at $k/(2\pi) \approx 1.44\,\mathrm{cm}^{-1}$ emerges in the spectrum.

The spectrum of the high frequency stripes peaks only once at $k/(2\pi) \approx 1.39\,\mathrm{cm}^{-1}$. This corresponds to a typical length scale $L \approx 0.72\,\mathrm{cm}$ of the pattern. In the second high frequency state, the peak shifts to a smaller wavenum-

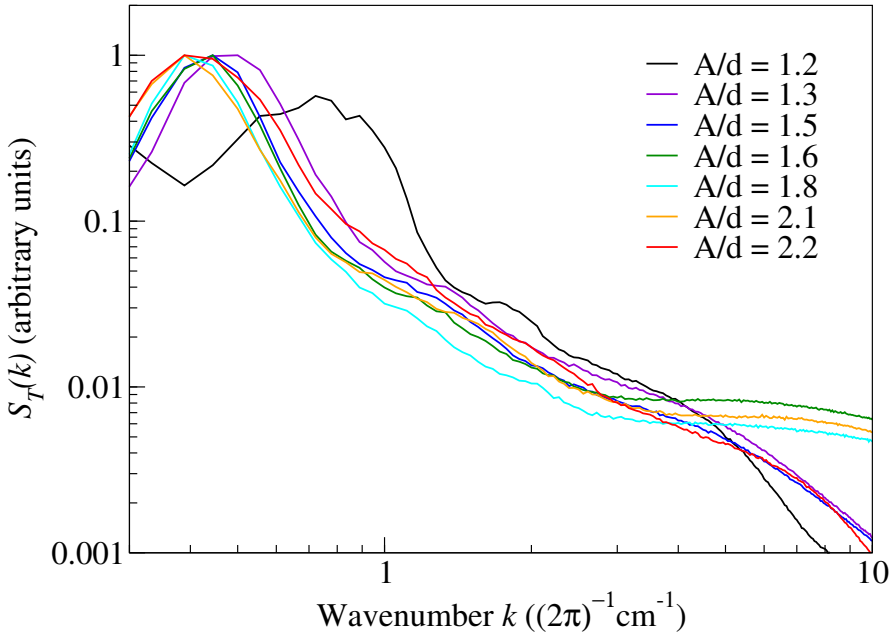

Figure 5.10: Power spectra of the topography for the low frequency stable stripes at different driving amplitudes obtained from the two-dimensional Fourier transform of short exposure photographs. The spectra were normalised such that the peak value equals unity. All spectra show one clear maximum. The position of the maximum moves to lower k-values with increasing driving amplitude.

ber $k/(2\pi) \approx 0.78\,\mathrm{cm}^{-1}$ such that the typical length scale of this pattern is $L \approx 1.28\,\mathrm{cm}$.

The spectrum of the turbulent state does not show any peaks, but is monotonically decreasing. Within small deviations the power spectrum can be described by a power-law with exponent $\alpha = -3.5$ in the range between $k/(2\pi) \approx 0.7\,\mathrm{cm}^{-1}$ and $k/(2\pi) \approx 0.9\,\mathrm{cm}^{-1}$; a power-law with $\alpha = -3.5$ is shown in Fig. 5.11 as a reference. The Kraichnan-Leith-Bachelor theory for two-dimensional turbulence predicts a scaling exponent of $\alpha_{\mathrm{theo}} = -3.0$ for the power spectrum of the kinetic energy $E(k)$ in the downscaling regime. Although these numbers are comparable, they refer to different observables.

Discussion

The spatial resolution of the analysis is limited: The discrete Fourier transform provides a step size of $\Delta k = 2\pi/L$, so that the length scales resolved are $\tilde{L} = L/n$,

$n \in \mathbb{N}$. Consequently, the spatial resolution for low k-values, that is large length scales, is not limited by the resolution of the camera but by the cell size. For high k-values, that is small length scales, noise due to reflections on individual particles and dust increases and we get close to the camera resolution. This appears as a cut-off in the spectrum at $k/(2\pi) \approx 10\,\mathrm{cm}^{-1}$. As this corresponds to length-scales much smaller than the typical length-scales of the patterns, it does not influence the measurements significantly.

During the data analysis artificial peaks induced by the lighting need to be identified. The very small peaks in the spectra of the low frequency crossrolls and the spatiotemporal chaos between $k/(2\pi) \approx 2\,\mathrm{cm}^{-1}$ and $k/(2\pi) \approx 4\,\mathrm{cm}^{-1}$ are likely to be residuals from shadows cast in the system that were not removed by the previous image processing. Our data do not allow us to decide, if the clear third peak in the spectrum of the spatiotemporal chaos corresponds to a third typical length scale in the pattern or if it is an artificial lighting-effect. To answer this questions the experiments would need to be repeated with a homogeneous lighting. Homogeneous lighting could be realised by using multiple light sources arranged symmetrically in a circle above the cell. Unfortunately this was not possible within the limits of this project.

Despite the experimental imperfections we can identify the characteristic length scales of the patterned states in the power spectra of the images (see Fig. 5.11). In contrast to the patterned states the power spectrum of the topography for the soft turbulent state shows a power-law-like behaviour. This suggests a coexistence of all length-scales resolved within our experimental precision. We obtain an exponent of $\alpha \approx -3.5$. Surprisingly, this is close to the theoretical prediction of the power spectrum of the kinetic energy $E(k)$ predicted by the Kraichnan-Leith-Bachelor theory for two-dimensional turbulence. It is by no means clear, how the measured spectrum $S_\mathrm{T}(k)$ is related to $E(k)$ in our system. A relation $S_\mathrm{T}(k) \propto E(k) \cdot k^x$, with $x = \mathrm{const}$ would be possible. Yet, the power-law-like behaviour strongly indicates that the system indeed descends into turbulence.

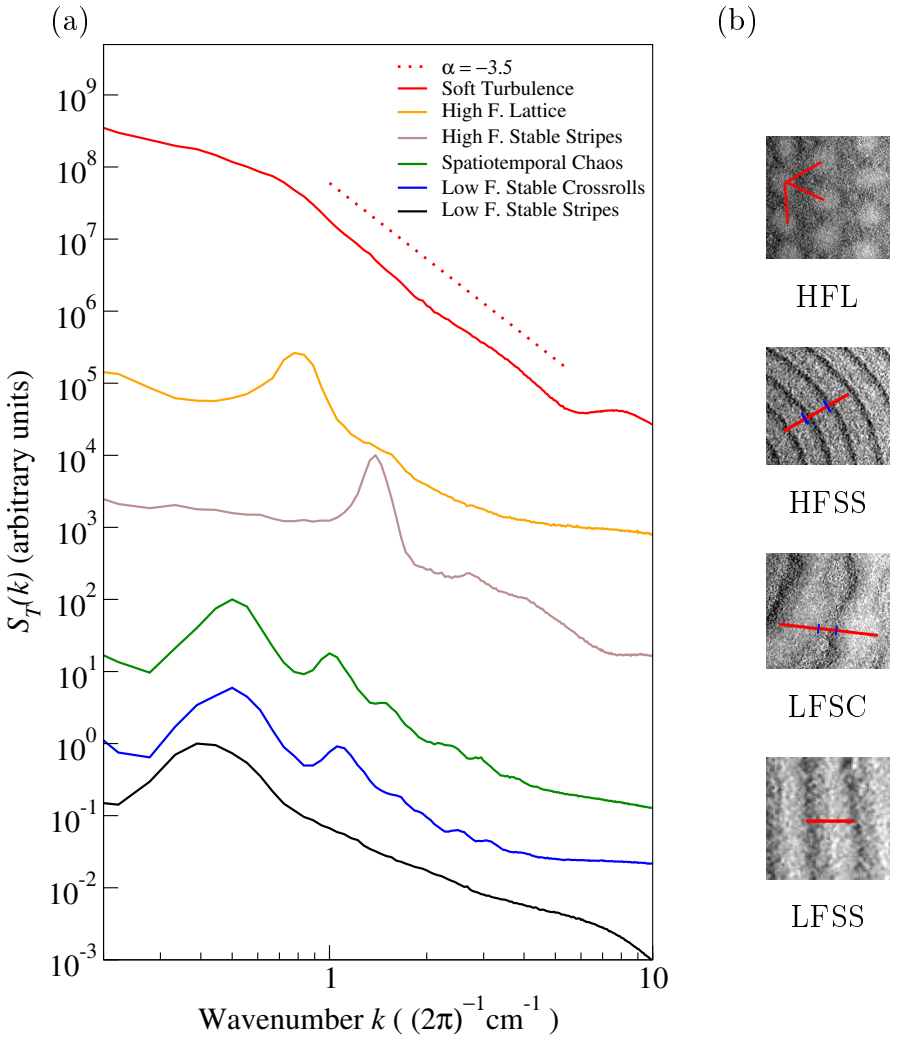

Figure 5.11: (a) Power spectra of the topography for the different states obtained from the two-dimensional Fourier transform of short exposure photographs. The driving frequency $f = 100\,\mathrm{Hz}$, and mean volume filling fraction $\phi \approx 34\,\%$ were kept constant. From bottom to top the driving amplitude are $2.2\,d$ (LFSS), $2.5\,d$ (LFSC), $2.7\,d$ (STC), 2.8 (HFSS), $2.9\,d$ (HFL) up to $3.3\,d$ (ST). The spectra were normalised such that the peak value equals unity. For the sake of clarity, the zero-point of the ordinate was shifted for the different spectra. The spectra of the low-frequency stable stripes, the high frequency stable stripes and the high frequency lattice pattern show each one clear maximum. The spectrum of the low frequency crossrolls shows two maxima, that is the pattern is characterised by two different length scales. The spectrum of the spatiotemporal chaos resembles the spectrum of the crossrolls, but shows additional minor peaks at higher wave-numbers. (b) Close-up images of the low frequency stable stripes, the low frequency crossrolls, the high frequency stripes and the high frequency lattice. The length scales corresponding to the peaks are marked in the images.

5.5 Frequency Spectra at Fixed Points in Space

In this section we characterise the inherent time-dependence of the different states at fixed position. Therefore we measure the power spectra of the time-evolution of the image intensity at fixed points in space $S_t(f)$. The intensity is correlated to the topography, that is to the mean height of the particles with respect to the cell, so that our measurements represent the time-evolution of the mean height at a fixed position. The data presented are obtained for a fixed volume filling fraction $\phi = 34\,\%$ and a fixed driving frequency $f_{\mathrm{shak}} = 100\,\mathrm{Hz}$.[4] The experiments were carried out in the large cell C_2.

Experimental Procedure

We use the sequences of images recorded with the high-speed camera for the measurements of the spatial power spectra of the topography. The experimental procedure is described in the previous section (Sect. 5.4). The time difference between two adjoining images of a sequence is $\Delta t = 2\,\mathrm{ms}$. For each state the amplitude was chosen such that the pattern fills the whole cell: $A \approx 2.0\,d$ (LFSS), ($A \approx 2.5\,d$ (LFSC), $A \approx 2.7\,d$ (STC), $A \approx 2.8\,d$ (HFSS) and $A \approx 2.9\,d$ (HFL).

Data Analysis

The images are cropped to the size of the cell and the light gradient is removed as described in Chap. 2. For each sequence of images we randomly choose 1000 image points (pixels) and record the image intensity at this point in time. We measure the power spectrum of the time-evolution of the intensity for each chosen image point by using the `fft`-function provided by `matlab`. We average over the spectra at the different image points and normalise the averaged spectra such that the peak value equals unity.

[4] For the sake of clarity we use the index "shak" throughout this section to mark the shaking frequency.

Results

Figure 5.12 shows the power spectra $S_t(f)$ for the low frequency stable stripes, the low frequency stable crossrolls, the spatio-temporal chaos and the high frequency stripes. The curves are nearly indistinguishable. The power spectra show a main maximum at $f_{pat} \approx 50\,\text{Hz} = f_{shak}/2$. Minor peaks can be found at harmonics of $f_{pat} = f_{shak}/2$. The value of the main maximum exceeds the minor maxima by more than one order of magnitude.

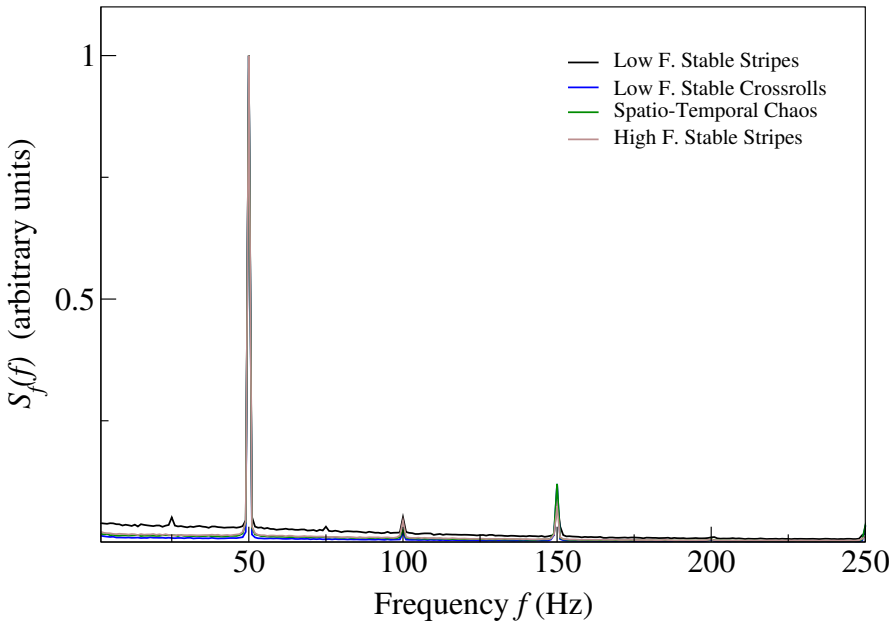

Figure 5.12: Normalised frequency spectra of arbitrarily chosen image points at a driving frequency $f_{driving} = 100\,\text{Hz}$ and filling fraction $\phi = 34\,\%$. The different curves correspond to different patterned states: low frequency stable stripes ($A \approx 2.0\,d$), low frequency crossrolls ($A \approx 2.5\,d$), spatio-temporal chaos ($A \approx 2.7\,d$) and high frequency stripes ($A \approx 2.8\,d$). The curves are nearly indistinguishable. One clear peak appears at $f_{pat} = 50\,\text{Hz} = f/2$, that is the patterns oscillate at half the driving frequency. Minor peaks appear at harmonics of f_{pat} and represent the shape of the signal.

In Fig. 5.13 the power spectra of the high frequency stripes and the high frequency lattice are shown. They differ significantly from each other: The spectrum of the high frequency lattice shows a main maximum at $f_{pat} = f_{shak}/3 \approx 33\,\text{Hz}$. Minor maxima appear at harmonics of $f_{pat} = f_{shak}/3$. The value of the first harmonic at $f = (2/3)f_{shak}$ is of the same order of magnitude as the value of the main

maximum. Additionally we observe a small peak at $f = 100\,\mathrm{Hz} = f_{\mathrm{shak}}$.

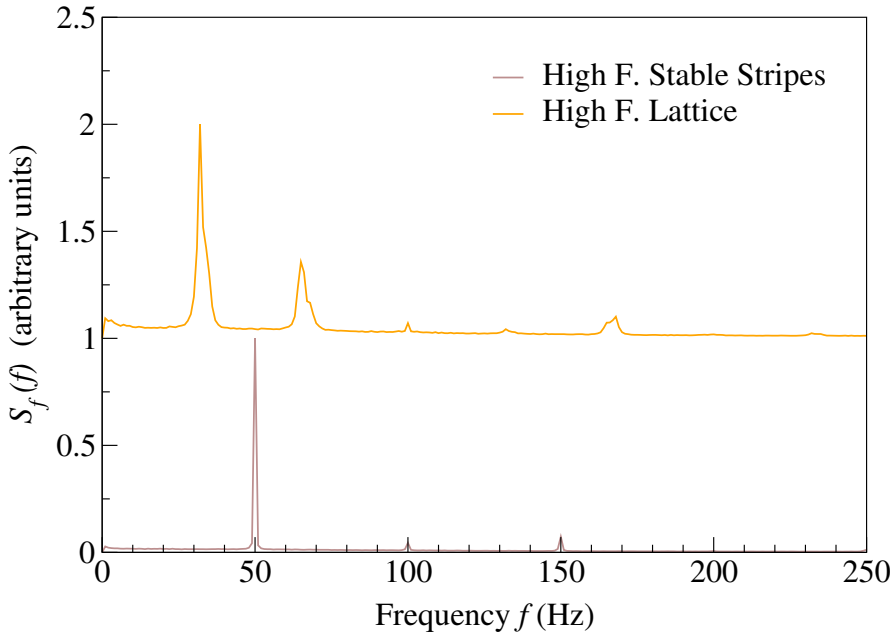

Figure 5.13: Normalised frequency spectra of arbitrarily chosen image points at a driving frequency $f_{\mathrm{driving}} = 100\,\mathrm{Hz}$ and filling fraction $\phi = 34\,\%$. The brown curve corresponds to the high frequency stable stripes ($A \approx 2.8\,d$) and the orange curve to the high frequency lattice ($A \approx 2.9\,d$). The zero-point of the ordinate axis was shifted for the high frequency lattice. The spectrum of the HFSS shows one clear main maximum at $f_{\mathrm{pat}} = 50\,\mathrm{Hz}$. Its spectral density exceeds the side maxima at harmonics of $f/2$ by one magnitude. The spectrum of the HFL has a main maximum at $f \approx 33\,\mathrm{Hz} \approx f/3$, a clear minor maximum at the first harmonic as well as less pronounced minor maxima at higher harmonics. The pronounced maximum at the first harmonic shows that the shape of the signal differs substantially from a perfect sine wave (see Fig. 5.16 and 5.15). Experimental parameters: $f_{\mathrm{driving}} = 100\,\mathrm{Hz}$, $A \approx 3.25\,d$, $\phi = 34\,\%$.

Discussion

The spectra presented were obtained from images, where a lighting gradient and also the mean brightness were removed. If we do not correct the data, the spectra change. Figure 5.14 shows the spectra of the high frequency stable stripes obtained from the raw, non-corrected image and from the lighting-corrected data. The spectrum of the non-corrected images shows a very pronounced maximum at a frequency equal to the driving frequency $f = f_{\mathrm{shak}} = 100\,\mathrm{Hz}$ as well as a pro-

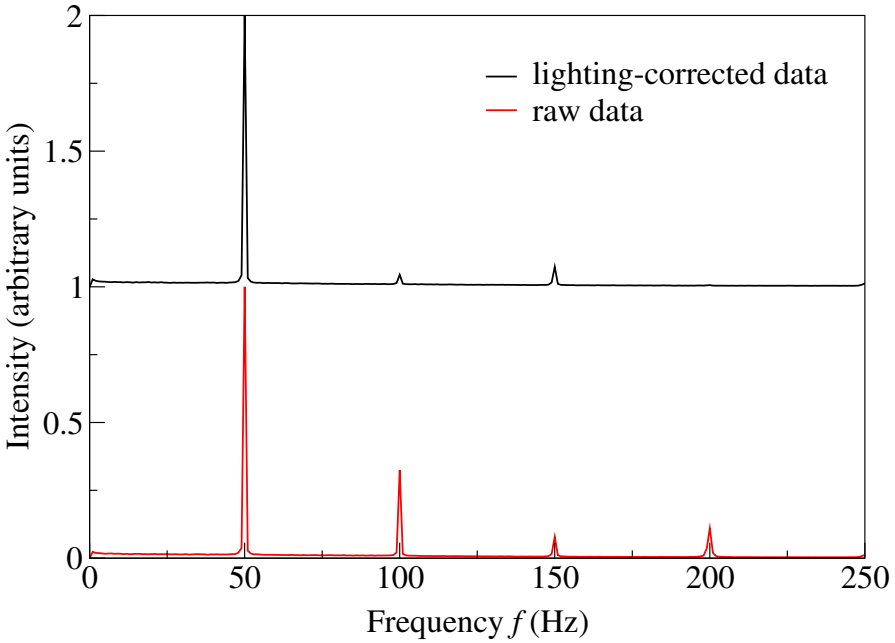

Figure 5.14: Frequency spectra of the high frequency stable stripes: The red curve shows the spectra of the raw image data, the black curve the spectra of the images after subtracting the intensity gradient. The spectra were normalised and the zero-point of the ordinate axis shifted. Experimental parameters: $f_{\mathrm{driving}} = 100\,\mathrm{Hz}$, $A \approx 2.8\,d$, $\phi = 34\,\%$.

nounced minor maximum at the first harmonic of the driving frequency $f = 200\,\mathrm{Hz}$. Both peaks are significantly smaller in the lighting-corrected images. This indicates that the vertical position of the cell influences mainly the mean brightness of an image.

All measured power spectra of the lighting-corrected images $S_{\mathrm{t}}(f)$ show a clear main maximum and several minor maxima at harmonics. The main maximum correspond to the frequency of the signal, whereas minor maxima show the shape of the signal. This is illustrated in Fig. 5.15. If the input signal is not a perfect sine, but a square wave, the Fourier transform does not show a single peak at the frequency, but minor peaks at even harmonics. Therefore the measurements reveal clearly the oscillation frequency of the standing waves that form the patterns: Except for the high frequency lattice pattern (HFL) all patterns oscillate at half the driving frequency. The period doubles with respect to the homogeneous state in which the particle layer follows the motion of the plates. The high frequency lattice pattern oscillates at a third of the driving frequency $f_{\mathrm{pat}} = f_{\mathrm{shak}}/3$. The period

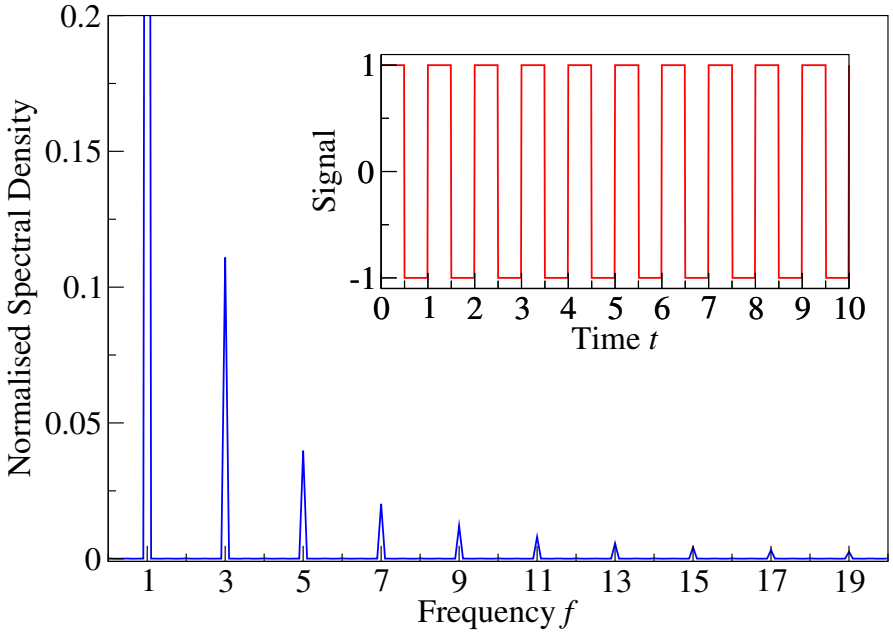

Figure 5.15: Normalised Fourier spectrum of a square wave with frequency $f = 1$. The input signal is shown in the inset. The spectral density was normalised such that the value of the main maximum (at $f = 1$) equals unity. The plot does not show the peak of the main maximum. Clear minor maxima can be found at even subharmonics $f = 1+2n$; $n \in \mathbb{N}$.

tripling is accompanied by a threefold symmetry in space: The hexagonal lattice can be modelled as a superposition of three plane waves of the same wavenumber at an angle of $\beta = 2\pi/3$ with respect to each other. Compared to the previous patterned states the period increases abruptly by 3/2. This discontinuity in the time-dependence of the oscillation coincides with a discontinuity in space: In contrast to all other patterns, the hexagonal lattice pattern develops independently of the high frequency stripes, whereas the other patterns develop through a smooth transition. It seems likely, that the discontinuity of the oscillation frequency cause the abrupt change in space.

The spectrum of the lattice pattern also shows more pronounced maxima at harmonics of the oscillation periods and a broadening of the peaks with respect to the former states. This shows that the oscillation differs significantly from a perfect sine wave. Figure 5.16 shows a typical extract of the time-evolution of the intensity at an arbitrarily chosen image point. As expected the signal is characterised

by a huge level of noise and a systematic asymmetry between the maxima and minima. The noise in the oscillation exceeds the noise in the oscillation of the previous pattern. The increase in the noise might be a precursor of the transition into turbulence when the driving amplitude is increased a little further.

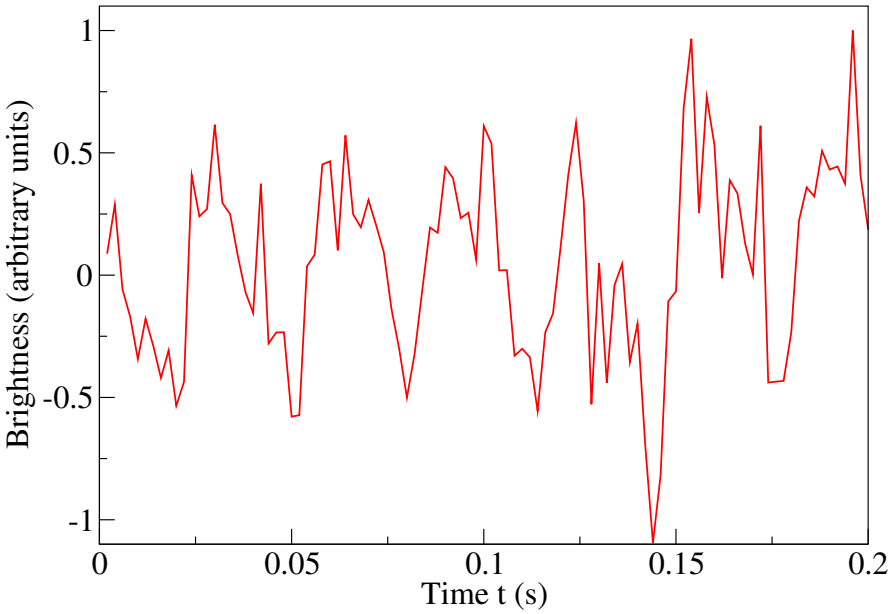

Figure 5.16: Time-evolution of the brightness of one arbitrarily chosen image-pixel at a driving frequency $f = 100\,\mathrm{Hz}$, driving amplitude $A = 2.9\,d$ and filling fraction $\phi = 34\,\%$. During the measurement, the high frequency lattice pattern filled the entire cell. The signal does not show a clear sine wave, but is overlaid by noise and slightly asymmetric. The asymmetry and the noise explain the spectral density of the harmonics in the spectrum shown in Fig. 5.13

Chapter 6

Discussion

In this chapter we discuss the relevant parameters of the system. We analyse the experimental imperfections of the system components and conclude with a short dimensional analysis to identify the relevant quantities.

6.1 Experimental Imperfections

Particles

We intended to work with a sample of monodisperse, spherical particles that interact solely through contact forces. The photomicrograph (Fig. 2.2) in Sect. 2.1 reveals that the particles vary significantly in shape and size. A less polydisperse sample would be preferable. The behaviour of the system depends crucially on the dryness of the particles: On humid days surface of the the particles is more wet, so that we observe a significant change in the behaviour. As an example, Fig. 6.1 shows a pattern that we observed only in the wet system. We could not observe a clear stripe-pattern or a hexagonal lattice pattern in the wet system. Instead labyrinthine patterns emerged and the system descended into a state very similar to the soft turbulence in the dry system at a driving amplitudes significantly lower than the instability threshold of the soft turbulent state in the dry system.

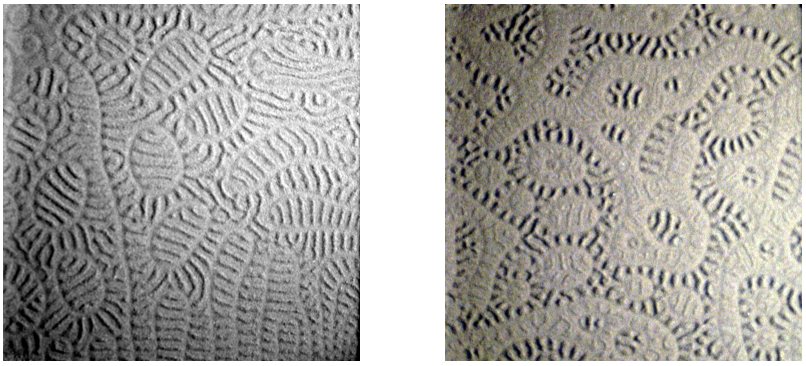

(a) (b)

Figure 6.1: Pattern observed in a slightly wet system at driving frequency $f = 100\,\mathrm{Hz}$, amplitude $A \approx 2\,d$ and filling fraction $\phi \approx 32.5\,\%$. The pattern corresponds to the low frequency crossroll-pattern in the dry system. The photographs were taken with long exposure time $T = 0.02\,\mathrm{s}$ (a) and short exposure time $T = 2\,\mathrm{ms}$ (b).

Cell

We could not observe a change in the pattern upon changing the material of the bottom plate (duraluminium and steel) or the material of the side walls (glass, duraluminium). Besides, the side length of the cell did not influence the phenomena significantly. The side length of the system should be relevant in containers with small aspect ratio, if $\gamma \sim 1$ or smaller; the influence of the side length should become negligible in the limit of high aspect ratios $\gamma \to \infty$. Although we used cells with large aspect ratio, we cannot neglect boundary effects: For example, the striped-patterns tend to align perpendicular to the side walls and spirals could only be observed in the cell with round corners.

We could also observe a strong dependence on the cell height on one occasion we unintentionally increased the cell height by approximately 1 mm by placing a stripe of spongy tape between the side walls and the bottom plate . In the higher cell a huge variety of patterned states, that cannot be observed in the low system, emerged. In our system, the height of the cell might vary slightly due to a bending of the bottom or top plate, but we assume that the variation is less than 0.1 mm. Inhomogeneities in the cell, e.g. in the bottom plate, might influence the different states, too. However, all states emerged independently of the cell used and the region, where they first emerged, as well as the shape varied upon every experi-

mental run. Besides, we could not observe a preferred direction in the large-scale circulation. This suggests that the phenomena may be influenced, but not caused, by inhomogeneities of the system.

Driving

The measurements with the accelerometer clearly show that the sinusoidal driving signal is overlaid with noise. The subharmonic standing waves, that is the pattern, should be destroyed if the noise exceeds a certain threshold. The experiments show that the phenomena are robust to small deviations from a perfect sinusoidal driving.
Nevertheless, inhomogeneities in the driving might provoke instabilities of higher order, due to hysteresis they can remain stable even below the instability threshold. If the noise is significantly higher at certain shaking amplitudes, for example, because of a resonance in the shaker, the plateaus of the instability curves could emerge (see Fig. 5.7). Spatial inhomogeneities in the shaking can cause the same effect and could be responsible for the observed coexistence of different states in carefully levelled cells. Both, spatial and temporal, inhomogeneities could be reduced by using a more powerful shaker with a head of equal and not smaller size than the cell.

Air Effects

The behaviour of the system might be influenced by the air flow around the particles, because the cells were not evacuated. The properties of the air, for example pressure, temperature and humidity, varied slightly due to weather changes. As Matas *et al.* [36] have shown, special subharmonic waves of rectangular profile, occur uniquely in the two-phase case of granular matter and a surrounding fluid. However, the surrounding fluid should become less important for higher densities of the particle material. The high density of bronze suggests, that air flow is negligible in the system studied.

Gravity

In the experiments, gravity introduces an asymmetry in the vertical direction. If the cell is not carefully levelled, the particles follow the slope and are likely to cause an avalanche. This illustrates the sensitivity of the system to gravity. With increasing driving acceleration, $\Gamma = A(2\pi f)^2$, levelling the cell becomes considerably easier. In the limit of high driving accelerations, gravitation should become negligible. Most of the experiments were carried out at peak accelerations ranging within $7 \leq \Gamma/g \leq 30$, such that the driving acceleration exceeds gravitation in most cases by one order of magnitude. Nevertheless, the frequency dependence of the soft turbulent state shows, that within the parameter range studied gravitation cannot be neglected.

6.2 Dimensional Analysis

The system can be described by a set of few parameters, if experimental imperfections like the polydispersity of the particles, inhomogeneities in the shaking, air flow, inhomogeneities in the cell construction and residual long-range interactions between the particles are neglected. The individual particles can be described by their diameter d, mass M_p; the cell geometry can be reduced to the height h and the side length L_0; the driving to the driving amplitude A and the frequency f. The particle-particle interactions and collisions with the cell boundaries can be modelled with the coefficients of restitution ε and $\varepsilon_\mathrm{boundary}$. The number of particles can be described by the mean volume filling fraction ϕ and gravity is characterized by the gravitational acceleration g. We assume, that the coefficient of restitution for collisions with the cell boundaries $\varepsilon_\mathrm{boundary}$ has only a negligible influence, because we did not observe a change in the system behaviour upon changing the material of the cell.
Consequently nine parameters, d, M_p, ε, h, L_0, A, f, ϕ and g, remain. The quantities can be expressed by three fundamental physical units, for example mass [kg], length [m] and time [s]. The Buckingham π theorem states that the parameter set can be reduced to $6 = 9 - 3$ dimensionless quantities. The mass of the particle M_p is the only quantity with a dimension of a mass, therefore it can be reduced

to 1. The coefficient of restitution ε and the mean volume filling fraction are expressed in dimensionless form already. The typical length scale could be set by the diameter of the particles. This allows to reduce d, h, L_0 and A to 1, h/d, L/d and A/d. Including gravity, we can reduce the gravitational acceleration g and the driving frequency f to 1 and $\Gamma/g := A(2\pi f)^2$.
In total we obtain one set of six dimensionless quantities ε, h/d, L_0/d, A/d, ϕ and Γ/g. Different, equivalent sets could be chosen. In the limit $L_0/d \to \infty$, this quantity can be neglected. As we observed all states in the small and the big cells, we assume, that the phenomena are nearly independent of the side length. This justifies the measurements taken for the phase diagram that were taken in cells with different aspect ratios.
If we assume that gravity is negligible, the nondimensionalization of Γ can not be carried out. The typical acceleration must then be written as $d(2\pi f)^2$ so that Γ reduces to A/d, too. This means the system's behaviour does not depend on the driving frequency and only ε, ϕ, h/d, (L_0/d) and A/d remain as relevant parameters.
Although the peak acceleration Γ exceeds gravity by about one order of magnitude, the instability thresholds of the turbulent states expressed in terms of the amplitude decrease monotonically with increasing driving frequency, whereas the shaking acceleration Γ/g of the instability thresholds seem to saturate, see Fig. 5.8. This suggests that gravity, though small compared to the driving acceleration, plays a crucial role.

Chapter 7

Conclusion and Outlook

The first part of this chapter contains a brief summary of the thesis. In the second part we put our research in context by comparing it to other pattern-forming systems. In the last part of this chapter we present ideas for future work.

7.1 Summary

The experimental set-up is simple: sand in a shaking box. Yet, the system shows two complex phenomena that are typical of far-from-equilibrium systems, phase separation and pattern-forming route to chaos.
The liquid-gas phase separation occurs at low filling fractions $\phi \leq 16\,\%$ and has been closely studied in a similar system [9, 12]; in our system, we could reproduce the observations qualitatively and parts of the measurements quantitatively within good approximation. At higher filling fractions $\phi \geq 15\,\%$ the system exhibits a set of patterned states as well as two distinct turbulent states. One of the turbulent states is characterised by remarkably pronounced waves ("soft turbulence"), the other by a large-scale circulation ("hard turbulence"). We successfully mapped out the stability regions of the different states for a fixed driving frequency in the parameter space spanned by the driving amplitude and the mean volume filling fraction.
We also presented preliminary results on the dependence of the phenomena on the driving frequency. The results suggest that gravity, though small compared to the

driving acceleration, plays a crucial role.
For a fixed filling fraction the system behaviour upon increasing the driving amplitude can be interpreted as a sequence of pattern-forming bifurcations that lead into turbulence. The different bifurcations show similarities to pattern formation in Rayleigh-Bénard convection, the Faraday experiment with molecular fluids and open-top granular systems. For one filling fraction we characterised nearly all states quantitatively with respect to their properties in space and time. The spatial power spectrum of the topography of the soft turbulent state strongly suggests that the system transition into fully developed turbulence. The temporal power spectra of the topography of the patterned states reveal that a period doubling and a period tripling with respect to the homogeneous state occurs.
Although the set-up is simple and the equations that determine the behaviour of an individual particle can easily be derived from classical mechanics, the emerging physics is rather complex.

7.2 Evaluation

With increasing driving amplitude the granular gas undergoes a sequence of pattern-forming bifurcations before descending into turbulence. The bifurcations are characterised by hysteresis, so that we observe a sequence of subcritical bifurcations. In this respect, they differ substantially from the pattern-forming bifurcations in the Faraday experiment (see Sect. 1.2), where the system undergoes supercritical bifurcations and the amplitude of the pattern varies continuously [14]. In granular open-top system both, supercritical and subcritical pattern-forming bifurcations have been reported [29, 72].
In our system, the bifurcations typically include a discontinuous change in the spatial frequency or the time-dependence. The primary and secondary patterns are stationary in time and show striking similarities with open-top granular systems, Faraday waves in viscous fluids and Rayleigh-Bénard convection. In all cases striped patterns emerge when the control parameter is increased slowly through the instability threshold. If the threshold is crossed abruptly, the coarsening dynamics are also similar to Faraday waves and Rayleigh-Bénard convection. It is now appreciated that the near-threshold dynamics close to the primary instability are

"universal in some sense" and independent of the details of the underlying mechanisms [14]. However, high energy dissipation rates, present in all three systems mentioned above, seem to play a crucial role in the formation of striped patterns, as no striped patterns can be observed in Faraday experiments with low-viscous fluids. Typically, the differences in the behaviour of different systems increase with increasing distance from the primary instability threshold. The secondary pattern in our system still shows striking similarities to the crossroll-instability that can be observed in Rayleigh-Bénard convection cells.

The third bifurcation introduces spatiotemporal chaos, a dynamical state in which the pattern evolves in an exceedingly complex way in our system. Spatiotemporally chaotic states have been observed in Rayleigh-Bénard convection and in the Faraday experiment, too. In both cases, these states are found only in systems that are sufficiently large. In cells with smaller aspect ratio, less disorganized patterns are found [14]. Measured in terms of numbers of particles or particle diameters, our experiment is incredibly small. Still we observe a complex, chaotic behaviour (see Sect. 5 and the video in the supplementary material, Sect. A.2). A further increase of the driving amplitude in our experiment restores a time-independent again, but the spatial frequency of the pattern increases abruptly.

Up to this point, all patterns oscillated at half the driving frequency. Consequently the primary instability induces a period doubling with respect to the homogeneous state where the granular layer follows the motion of the plates. Similar frequency dependence is usually observed in open-top granular systems and Faraday waves. In these systems higher instabilities often induce another period doubling, that is patterns oscillating with $f/4$. In contrast the next bifurcation in our system produces a pattern with an oscillation period of three times the driving period - a period tripling with respect to the homogeneous state and an increase by $3/2$ with respect to the previous patterned states. A pattern oscillating with $f/3$ has been observed in a wet granular system [72]. In both systems, the threefold symmetry in time is coupled with a threefold symmetry in space: The wet granular system shows a three-armed rotating spiral, our dry system develops a hexagonal lattice, that is the superposition of three standing plane waves. In the wet granular system, the pattern with arises from the homogeneous state, so that indeed a period tripling occurs. In contrast, in our system, the pattern oscillating with $f/3$ succeeds a

pattern oscillating with $f/2$.
Although several sequences of period-doubling in pattern-forming granular systems have been studied, experimental observations of a transition to turbulent states have not been reported yet. In contrast, our system transitions into a state in which we observe dramatic waves destroying the patterns. The measured power spectrum of the topography $S_{\mathrm{T}}(k)$ provides evidence of turbulence, so that we most likely observe the full pattern-forming bifurcation route to turbulence.
This assumption goes in line with an observation prior to this work when the experiment was carried out with glass particles: The particles charged up very quickly as soon as the system transitions into the wave-like state. This indicates a significantly higher collision rate than in the patterned states and as such a significant increase of the dissipation rate. A high dissipation rate is also one of the characteristic feautures of turbulence in molecular fluids.
Counterintuitively, a further increase of the driving amplitude restores spatial and temporal coherence in form of a large scale circulation. This phenomenology is strongly reminiscent of the transitions to soft and hard turbulence in Rayleigh-Bénard convection.
In summary the route of pattern-forming bifurcations leading to turbulent-like states that we observe combines a mixture of universality, that is independence from the details of the interactions, and uniqueness, that makes it a most fascinating subject and suggests, that a closer study of the phenomena might provide a deepened understanding of universal pattern-forming behaviour.

7.3 Outlook

During the course of the experiments several questions arose that could not be answered within the limited time scale. For example we have observed pattern formation and turbulence at different frequencies, but did not thoroughly study the frequency dependence of all states. Closely related to the frequency dependence is the impact of gravity that needs to be clarified. In numerical simulations gravity could be varied arbitrarily. It would be interesting to test if the patterned states and turbulence can be observed without gravity and how gravity effects the shape. Besides, the system has shown to react sensitively to a change of the cell height.

A systematic variation of the cell height is yet to be carried out and likely to allow the observation of a great variety of different patterns.
Although the energy is injected in the third dimension and the patterns correspond to the topography, that is a variation in the third dimension, the system studied seems to behave as a two-dimensional gas: In the phase coexistence the interface minimised equals a line-interface and the exponent measured in the turbulent region is closer to Kraichnan-Leith-Bachelor-scaling for two-dimensional turbulence than to exponents predicted for and measured in three-dimensional turbulence. A variation of the height invites the question "Where is the transition from two-dimensionality to three-dimensionality?"

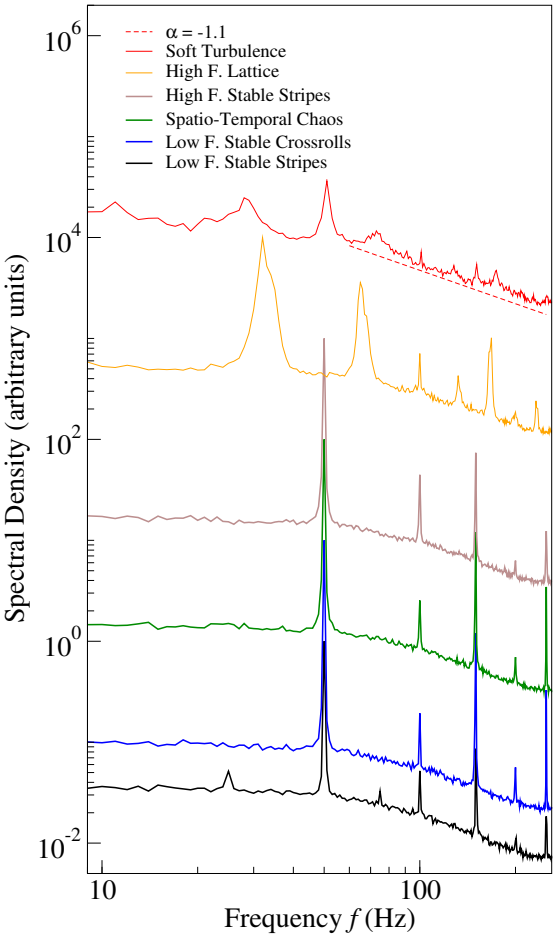

Figure 7.1: Power spectra of the topography-evolution in time $S_f(f)$ in arbitrary units. The zero-point of the ordinate axis was shifted for the different curves. The different, continuous curves correspond to the different states. The spectra of the patterned states are described in Sect. 5.5 and show the oscillation frequency of the patterns. The spectrum of the soft turbulent states shows maxima at $f_{\mathrm{shak}}/3$ and $f_{\mathrm{shak}}/2$ and harmonics of them. These maxima can be explained, because the data were obtained at an amplitude, where the patterns (high frequency stable stripes and high frequency lattice) still underlie the waves. At higher frequencies $f > 50\,\mathrm{Hz}$, the spectrum resembles a power-law decay. As a guide to the eye, the dotted red-line shows a power-law decay with a scaling exponent $\alpha = -1.1$.

The power-law dependence of the image spectra of the soft turbulent state as well as the similarities to turbulence in Rayleigh-Bénard Convection and Faraday ex-

periments strongly suggests that the system descends into turbulence. Further evidence of turbulence might be obtained by extending the analysis performed in Sect. 5.5 for the patterned states to the soft and hard turbulence, that is by measuring the power spectrum of the topography-evolution in time at a fixed point in space $S_f(f)$ (see Sect. 5.5). The data presented in Sect. 5.5 were obtained from sequences of images recorded with the high-speed camera that were originally intended only as additional material to illustrate the pattern-forming mechanism. Because of overheating of the shaker, we could only record a sequence of images at a driving amplitude where the soft turbulence is not fully developed. As the video in the supplementary material (see Sect. A.2) shows, patterns still underlie the waves. Due to the limited time-scale of the Bachelor's project, the measurements could not be repeated. We analysed the data as described in Sect. 5.5. Figure 7.1 shows the measured spectrum $S_f(f)$ of the (not fully developed) turbulent state in comparison to the patterned states. The spectrum shows two main maxima at $f_{\mathrm{shak}}/3$ and $f_{\mathrm{shak}}/2$ and minor maxima at harmonics of these frequencies. These peaks must be attributed to the underlying patterns. At higher frequencies $f > 50\,\mathrm{Hz}$, the spectrum is very noisy, but suggests a power-law decay with an exponent of $\alpha = 1.1$. From bottom to top in Fig. 7.1, that is with increasing driving amplitude, it looks as if the system transitions into a state with no typical time scale. The data are too noisy to state the evolution into a power-law-like behaviour, but hint that by averaging over more measurements evidence of a power-law-dependence can be obtained. This would be further evidence of turbulence. To compare the measured spectrum $S_{\mathrm{f}}(f)$ with theoretical predictions $E(k)$, the relation of the topography and the energy, as well as the dispersion relation between f and k would need to be ascertained. This might be difficult in experiments, but all quantities can be calculated in numerical simulations.

If the system should prove to be turbulent, then we might ask the question "What changes in the behaviour of individual particles, when the system transitions to turbulence?" This task is much easier to tackle in a granular system of macroscopic particles than in molecular fluids. This approach to turbulence has been treated only scarcely for molecular fluids [73], but might provide a new insight to "one of the last unsolved problems of classical mechanics" [66].

Appendix A

Appendix

A.1 Engineering Sketches of the Big Cell

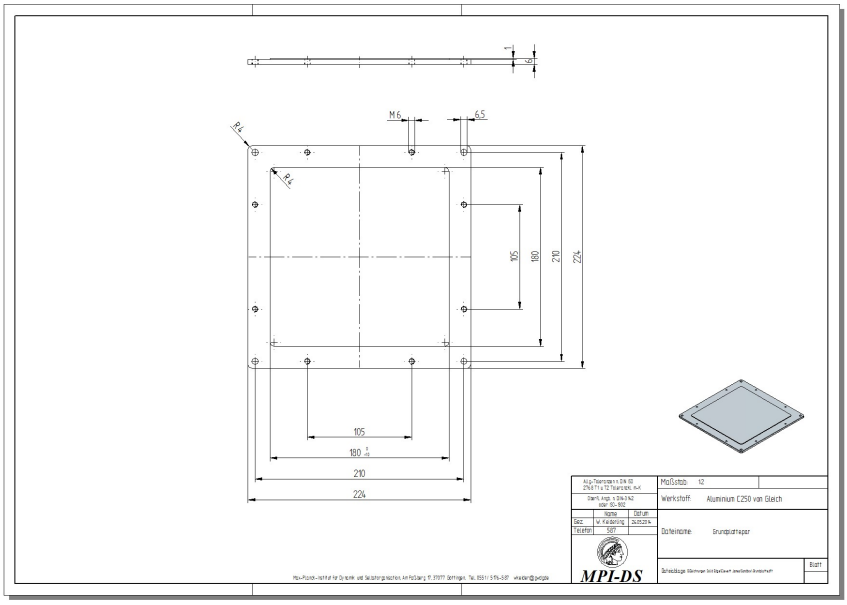

(a) bottom plate

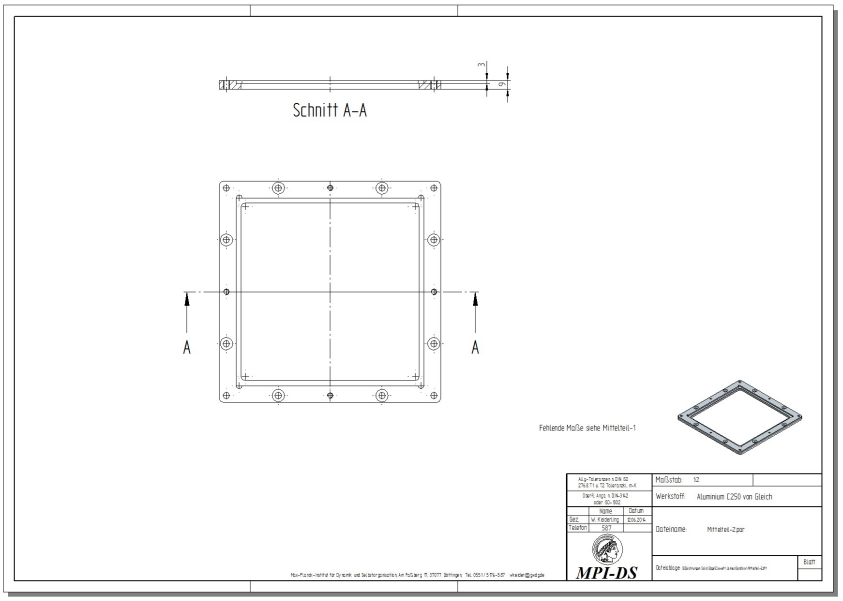

(b) one-piece side walls

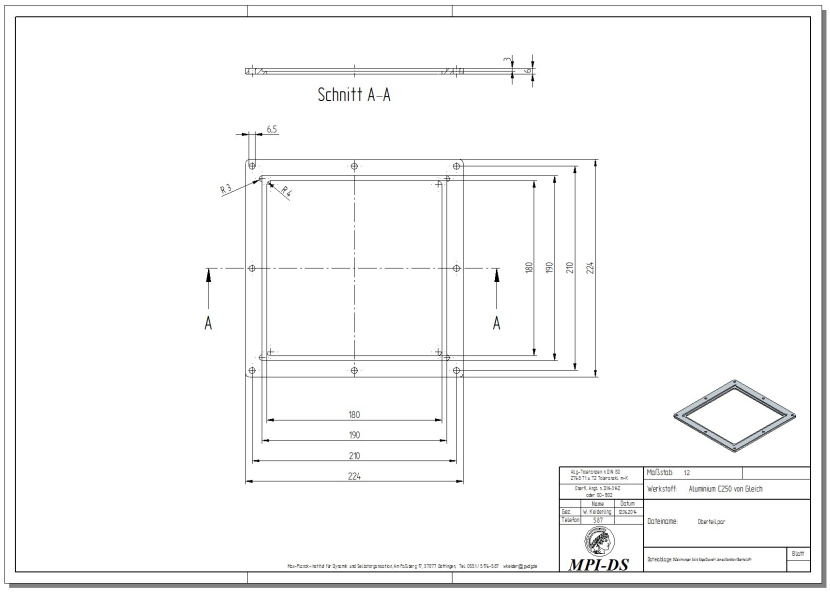

(c) frame

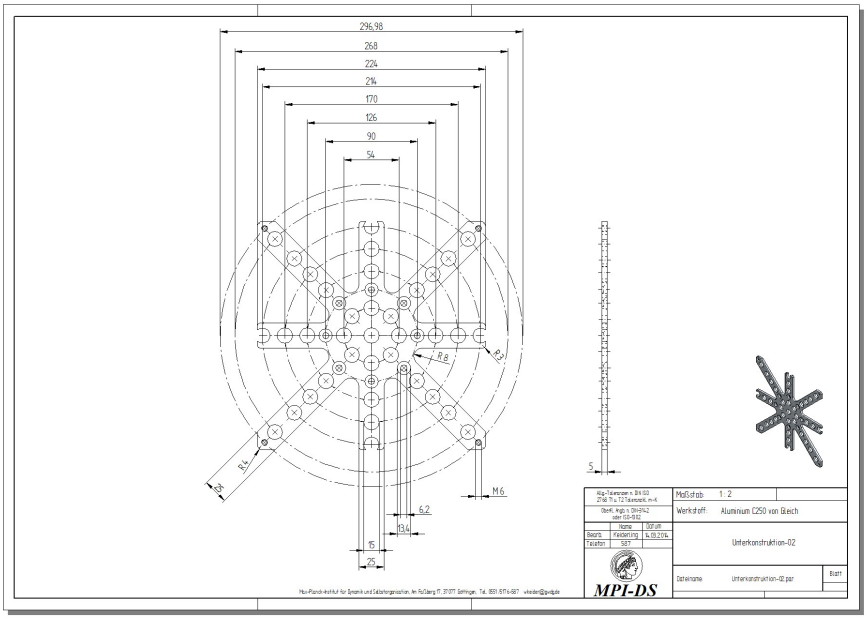

(d) substructure

Figure A.1: Engineering sketches of the different components of the big cell: the bottom plate (a), the one-piece side walls (b), the frame (c) and the substructure (d). The numbers denote the dimensions in mm.

A.2 Videos in the Supplementary Material

The supplementary material contains two sets of videos and a visualization of the large-scale circulation. All movies can be found in the public folder of the MPI-DS computer "vegan": "/scratch.local/data/public/sreimers/videos".
One set of videos shows the dynamics in the cell C_3 with a filling fraction of $\phi = 40\,\%$ at normal speed. The frequency was kept constant at $f = 100\,\mathrm{Hz}$. The amplitude was increased abruptly from $A = 0\,d$ to a target amplitude $A \neq 0\,d$. A short description of the videos is given in Tab. A.1.
The other set of videos contains slow-motion movies of the different states. The images were taken with the `PCO-1200s Camera` at the maximal frame rate of the camera $500\,\mathrm{s}^{-1}$. The speed of the movie is $3\,\%$ of the original time. The videos show the cell C_1 with a filling fraction of $34\,\%$. Within the time recorded, the frequency and the amplitude were kept constant at $f = 100\,\mathrm{Hz}$ and at the target amplitude which is specified in Tab. A.2.
The movie of the large-scale circulation (filename: LSC.avi) is obtained from photographs taken with the `Olympus Digital E 500 camera` at a constant frame rate of $2.5\,\mathrm{s}^{-1}$. The playback speed of the video is four times of the original speed. The experiment was carried out in the small cell C_2 with a filling fraction of $\phi = 40\,\%$ at a driving frequency of $f = 100\,\mathrm{Hz}$ and an amplitude of $A = 4.25\,d$. We used a steel tracer particle to visualize the flow.

Normal-Speed Videos	
Filename	**Description**
LFSS_ 1.5.MP4	Coarsening dynamics of the LFSS: At the beginning, the pattern shows several defects and droplets. With increasing time the defects and droplets disappear and a line-pattern remains. The lines align perpendicular to the side-walls.
STC_ 2.6.MP4	Dynamics of the STC: The motion grows from the centre of the cell. Small droplets emerge rapidly and either merge with a neighbouring stripe or disappear. The stripes shiver or move.
HFSS_ 2.7.MP4	Coarsening dynamics of the HFSS: At the beginning, the pattern emerges as a defect-line pattern and shows small droplets in the centre. With increasing time, the droplets and the defects disappear. In the middle of the movie, the LFSC-pattern emerges in the centre of the cell, probably because the cell was slightly unlevel or because of an inhomogeneity in the driving.
ST_ 2.8.MP4	Waves in the soft turbulent state slightly above the instability threshold. Patterns still underlie the waves.
ST_ 3.0.MP4	Waves in the soft turbulent state in the fully developed turbulent regime. The waves have destroyed the patterns completely.

Table A.1: Overview of the normal-speed videos. The number in the filename indicates the driving amplitude in particle diameters d. All experiments were carried out in the cell C_3 at a driving frequency $f = 100\,\mathrm{Hz}$ and a mean volume filling fraction $f = 40\,\%$. The videos show the dynamics following a jump of the driving amplitude from $A = 0\,d$ to the target amplitude specified in the table.

Slow-Motion Videos	
Filename	**Description**
Prepattern_ 0.9.avi	Dynamics of the "Pre-pattern". The amplitude was increased slowly from below the fluidisation point to the target amplitude.
LFSS_ 1.5.avi	The LFSS forming a spiral. If the video is shown at normal speed, the pattern looks stationary in time.
LFSS_ 2.0.avi	The LFSS forming circles.
LFSC_ 2.5.avi	The LFSC developing out of a LFSS-pattern forming circles. The amplitude was increased slowly above the second instability threshold. The bifurcation emerged as the additional droplets in the centre of the circles.
LFSC_ 2.6.avi	The LFSC developing out of a LFSS-pattern forming a spiral. The amplitude was increased slowly above the second instability threshold.
STC_ 2.7.avi	Spatiotemporal chaos developing out of a spiral structure.
HFSS_ 2.8.avi	HFSS-pattern following a slow increase of the driving amplitude.
HFL_ 2.9.avi	HFL-pattern following a slow increase of the driving amplitude.
ST_ 3.0.avi	Soft turbulence near the instability threshold. Patterns still underlie the waves.

Table A.2: Overview of the slow-motion videos. The number in the filename indicates the driving amplitude in particle diameters d. All experiments were carried out in the large cell C_1 at a driving frequency $f = 100\,\mathrm{Hz}$ and a mean volume filling fraction $\phi = 34\,\%$. The total time of one movie corresponds to 1 s.

References

[1] *Photograph of geological formations in the desert*, http://nature.desktopnexus.com/wallpaper/527524/.

[2] *Photograph of patterns on sand dunes*, http://wallpaperscraft.com/download/desert_sand_dunes_pattern_4914.

[3] *Photograph of giraffe hide*, http://de.forwallpaper.com/wallpaper/baby-giraffe-613557.html.

[4] N. V. Brilliantov and T. Pöschel, *Kinetic theory of granular gases*, Oxford Graduate Texts (OUP Oxford, 2004).

[5] P. Richard, M. Nicodemi, R. Delannay, P. Ribiere, and D. Bideau, "Slow relaxation and compaction of granular systems", Nature Materials **4**, 121 (2005).

[6] L. Mester, *The new physical-mechanical theory of granular materials* (Homonnai, 2009).

[7] H. M. Jaeger, S. R. Nagel, and R. P. Behringer, "Granular solids, liquids, and gases", Reviews of Modern Physics **68**, 1259 (1996).

[8] J. S. Olafsen and J. S. Urbach, "Clustering, order, and collapse in a driven granular monolayer", Physical Review Letters **81**, 4369 (1998).

[9] K. Roeller, J. P. D. Clewett, R. M. Bowley, S. Herminghaus, and M. R. Swift, "Liquid-gas phase separation in confined vibrated dry granular matter", Physical Review Letters **107**, 048002 (2011).

[10] Prevost, Melby, Egolf, and Urbach, "Nonequilibrium two-phase coexistence in a confined granular layer", Physical Review Letters **107**, 507 (2004).

[11] F. Vega Reyes and J. S. Urbach, "Effect of inelasticity on the phase transitions of a thin vibrated granular layer", Physical Review E **78**, 051301 (2008).

[12] J. P. D. Clewett, K. Roeller, R. M. Bowley, S. Herminghaus, and M. R. Swift, "Emergent surface tension in vibrated, noncohesive granular media", Physical Review Letters **109**, 228002 (2012).

[13] M. C. Cross and P. C. Hohenberg, "Pattern-Formation outside of equilibrium", Reviews of Modern Physics **65**, 851 (1993).

[14] M. Cross and H. Greenside, *Pattern formation and dynamics in nonequilibrium systems* (Cambridge University Press, 2009).

[15] D. M. Winterbottom, *Pattern formation with a conservation law*, PhD thesis, University of Nottingham (2005).

[16] F. H. Busse and J. Whitehead, "Instabilities of convection rolls in a high prandtl number fluid", Journal of Fluid Mechanics **47**, 305 (1971).

[17] A. C. Newell, T. Passot, and J. Lega, "Order parameter equations for patterns", Annual Review of Fluid Mechanics **25**, 399 (1993).

[18] P. Manneville, *Instabilities, chaos and turbulence*, ICP fluid mechanics (Imperial College Press, 2010).

[19] E. Bodenschatz, W. Pesch, and G. Ahlers, "Recent developments in Rayleigh-Benard convection", Annual Review of Fluid Mechanics **32**, 709 (2000).

[20] S. W. Morris, E. Bodenschatz, D. S. Cannell, and G. Ahlers, "The spatio-temporal structure of spiral-defect chaos", Physica D **97**, 164 (1996).

[21] E. Brown, A. Nikolaenko, and G. Ahlers, "Reorientation of the large-scale circulation in turbulent rayleigh-bénard convection", Physical Review Letters **95**, 084503 (2005).

[22] D. Funfschilling and G. Ahlers, "Plume motion and large-scale circulation in a cylindrical rayleigh-bénard cell", Physical Review Letters **92**, 194502 (2004).

[23] E. Brown and G. Ahlers, "Large-scale circulation model for turbulent rayleigh-bénard convection", Physical Review Letters **98**, 134501 (2007).

[24] S. Douady, "Experimental-study of the Faraday instability", Journal of Fluid Mechanics **221**, 383 (1990).

[25] W. Edwards and S. Fauve, "Patterns and quasi-patterns in the Faraday experiment", Journal of Fluid Mechanics **278**, 123 (1994).

[26] M. Faraday, "On the forms and states assumed by fluids in contact with vibrating elastic surfaces", Philosophical Transactions of the Royal Society **121**, 319 (1831).

[27] D. Levine and P. Steinhardt, "Quasicrystals - a new class of ordered structures", Physical Review Letters **53**, 2477 (1984).

[28] S. Douady, S. Fauve, and C. Laroche, "Subharmonic instabilities and defects in a granular layer under vertical vibrations", Europhysics Letters **8**, 621 (1989).

[29] C. Bizon, M. D. Shattuck, J. B. Swift, W. D. McCormick, and H. L. Swinney, "Patterns in 3D vertically oscillated granular layers: Simulation and experiment", Physical Review Letters **80**, 57 (1998).

[30] P. Eshuis, K. van der Weele, M. Alam, H. J. van Gerner, M. van der Hoef, H. Kuipers, S. Luding, D. van der Meer, and D. Lohse, "Buoyancy driven convection in vertically shaken granular matter: experiment, numerics, and theory", Granular Matter **15**, 893 (2013).

[31] J. R. de Bruyn, B. C. Lewis, M. D. Shattuck, and H. L. Swinney, "Spiral patterns in oscillated granular layers", Physical Review E **63**, 1 (2001).

[32] Yonggun Jun, Kipom Kim, and Hyuk Kyu Pak, "Transient spiral and target patterns in vertically oscillated thin granular layers", in AIP Conference Proceedings, Stochastic Dynamics and Pattern Formation in Biological and Complex Systems. APCTP Conference, 7-10 July 1999, Seoul, South Korea (Asia Pacific Center for Theor. Phys. and Centre for Neurodynamics and et al, 2000), p. 43.

[33] F. Melo, P. B. Umbanhowar, and H. L. Swinney, "Transition to parametric wave patterns in a vertically oscillated granular layer", Physical Review Letters **72**, 172 (1994).

[34] P. B. Umbanhowar, F. Melo, and H. L. Swinney, "Periodic, aperiodic, and transient patterns in vibrated granular layers", Physica A **249**, 1 (1998).

[35] P. Eshuis, K. van der Weele, D. van der Meer, R. Bos, and D. Lohse, "Phase diagram of vertically shaken granular matter", Physics of Fluids **19**, 123301 (2007).

[36] J. P. Matas, J. Uehara, and R. P. Behringer, "Gas-driven subharmonic waves in a vibrated two-phase granular material", European Physical Journal E **25**, 431 (2008).

[37] P. B. Umbanhowar, F. Melo, and H. L. Swinney, "Localized excitations in a vertically vibrated granular layer", Nature **382**, 793 (1996).

[38] J. R. de Bruyn, C. Bizon, M. D. Shattuck, D. Goldman, J. B. Swift, and H. L. Swinney, "Continuum-type stability balloon in oscillated granular layers", Physical Review Letters **81**, 1421 (1998).

[39] F. Melo, P. B. Umbanhowar, and H. L. Swinney, "Hexagons, kinks and disorder in oscillated granular layers", Physical Review Letters **75**, 3838 (1995).

[40] Y. H. Taguchi and H. Takayasu, "Power-law velocity fluctuations due to inelastic-collisions in numerically simulated vibrated bed of powder", Europhysics Letters **30**, 499 (1995).

[41] Y. H. Taguchi, "New origin of a convective motion - elastically induced convection in granular-materials", Physical Review Letters **69**, 1367 (1992).

[42] M. Isobe, "Granular turbulence in two dimensions: Microscale Reynolds number and final condensed states", International Journal of Modern Physics C **23**, 1250032 (2012).

[43] M. Lesieur, *Turbulence in fluids*, Fluid Mechanics and Its Applications (Springer, 2008).

[44] *Photograph of a turbulent jet*, http://www.forwind.de/forwind/index.php?article_id=94&clang=1.

[45] *False-colour image of Jupiter's Great Red Spot (Voyager 1)*, Office of Public Information, Jet Propulsion Laboratory, California Institute of Technology, National Aeronautics and Space Administration http://nssdc.gsfc.nasa.gov/photo_gallery/photogallery-jupiter.html.

[46] A. N. Kolmogorov, "The local structure of turbulence in incompressible viscous fluid for very large Reynolds numbers", Doklady Akademii Nauk **30** (1941).

[47] R. Bolgiano, "Turbulent spectra in a stably stratified atmosphere", Journal of Geophysical Research **64**, 2226 (1959).

[48] A. Obukhov, "Effect of archimedean forces on the structure of the temperature field in a turbulent flow", Doklady Akademii Nauk **125**, 1246 (1959).

[49] R. H. Kraichnan, "Inertial ranges in two dimensional turbulence", Physics of Fluids **10**, 1417 (1967).

[50] C. E. Leith, "Diffusion approximation for two dimensional turbulence", Physics of Fluids **11**, 671 (1968).

[51] G. K. Batchelor, "Computation of the energy spectrum in homogeneous, two dimensional turbulence", Physics of Fluids **12**, II–233 (1969).

[52] E. Gkioulekas, *A theoretical study of the cascades of 3D, 2D, and QG turbulence*, PhD thesis, University of Washington (2006).

[53] R. H. Kraichnan, "Inertial range transfer in two and three dimensional turbulence", Journal of Fluid Mechanics **47**, 525 (1971).

[54] G. Boffetta, "Energy and enstrophy fluxes in the double cascade of two-dimensional turbulence", Journal of Fluid Mechanics **589**, 253 (2007).

[55] J. Paret and P. Tabeling, "Experimental observation of the two-dimensional inverse energy cascade", Physical Review Letters **79**, 4162 (1997).

[56] E. E. Siggia and H. Aref, "Point-vortex simulation of the inverse energy cascade in 2-dimension turbulence", Physics of Fluids **24**, 171 (1981).

[57] U. Frisch and P. L. Sulem, "Numerical simulation of the inverse cascade in two-dimensional turbulence", Physics of Fluids **27**, 1921 (1984).

[58] V. Borue, "Inverse energy cascade in stationary 2-dimensional homogeneous turbulence", Physical Review Letters **72**, 1475 (1994).

[59] S. Succi, P. Santangelo, and R. Benzi, "High-resolution lattice-gas simulation of two-dimensional turbulence", Physical Review Letters **60**, 2738 (1988).

[60] H. Kellay, X. L. Wu, and W. I. Goldburg, "Experiments with turbulent soap films", Physical Review Letters **74**, 3975 (1995).

[61] T. Gotoh, "Energy spectrum in the inertial and dissipation ranges of two-dimensional steady turbulence", Physical Review E **57**, 2984 (1998).

[62] E. Lindborg and K. Alvelius, "The kinetic energy spectrum of the two-dimensional enstrophy turbulence cascade", Physics of Fluids **12**, 945 (2000).

[63] K. Nam, E. Ott, T. Antonsen, and P. Guzdar, "Lagrangian chaos and the effect of drag on the enstrophy cascade in two-dimensional turbulence", Physical Review Letters **84**, 5134 (2000).

[64] F. Zöllner, *Leonardo da Vinci: Sketches and Drawings* (Taschen, 2004).

[65] CMI, *Millenium problems*, http://www.claymath.org/millennium-problems.

[66] J. C. Baez, *Open questions in physics*, Retrieved March 7, 2011, University of California, Riverside: Department of Mathematics, 2006.

[67] J. W. Cahn and J. E. Hilliard, "Free energy of a nonuniform system 1. Interfacial free Energy", Journal of Chemical Physics **28**, 258 (1958).

[68] P. C. Hohenberg and B. I. Halperin, "Theory of dynamic critical phenomena", Reviews of Modern Physics **49**, 435 (1977).

[69] P. K. Mishra, *Instabilities and turbulence in Rayleigh-Bénard convection: Numerical and phenomenological studies*, PhD thesis, Indian Institute of Technology Kanpur (2010).

[70] M. K. Rivera, *The inverse energy cascade of two-dimensional turbulence*, PhD thesis, University of Pittsburgh (2000).

[71] K. E. Daniels and M. Schroeter, "Focus on granular segregation", New Journal of Physics **15**, 1 (2013).

[72] K. Huang and I. Rehberg, "Period tripling causes rotating spirals in agitated wet granular layers", Physical Review Letters **107**, 028001 (2011).

[73] N. Francois, H. Xia, H. Punzmann, S. Ramsden, and M. Shats, "Three-dimensional fluid motion in Faraday Waves: Creation of vorticity and generation of two-dimensional turbulence", Physical Review X **4**, 021021 (2014).

Acknowledgements

This project would not have been possible, if it were not for the help and support of many people. Unfortunately, I cannot mention all of them individually in this context, because otherwise the length of this chapter would exceed the length of the whole thesis; for the sake of the environment, I have to limit the number of pages.

I want to express my deepest gratitude to my supervisor, Marco G. Mazza, who enabled me to join his group for working on this project. With his broad knowledge, he offered most helpful guidance when required, but he also granted me liberty with respect to the choice and design of the project. I want to thank him for the kind support and his willingness to give his time so generously.

My very special thanks I want to offer to James Clewett. We shared an incredibly huge amount of time in the lab - including Sunday afternoons - and most of the time, I enjoyed it very much. With his experimental and theoretical experience, he pushed the progress of the project extremely. During my rare moments of depression, James' optimism and ideas soon restored my good mood. I want to thank James for the great time we had, for the laboratory skills he taught me and especially for his enthusiasm about a "most simple"[1] far-from-equilibrium thermodynamic system. Gradually, I have (at least partially) adopted this enthusiasm.

This project would have been far less enjoyable, if it were not for the great atmosphere in the DCF-department in general and especially in the yellow floor. I want to thank Stephan Herminghaus for establishing this cordial environment. Frequent discussions with several people have helped me a lot. Besonders möchte ich in diesem Zusammenhang Mathias Hummel für die Hilfestellungen und leb-

[1] After all, it is nothing but sand in box...

haften Diskussionen, sowie für sein „Zweifeln an der Turbulenz“ danken.
Mein ganz besonderer Dank gilt Matthias Schröter. Er hat mir nicht nur das Labor zur Verfügung gestellt, sondern mir auch bei experimentellen Problemen mit Rat, Tat und vor allem der nötigen Ruhe geholfen.
Auf keinen Fall vergessen möchte ich all jene, ohne die das Projekt nicht möglich gewesen wäre: Da wäre zum Beispiel Wolf Keiderling und die Forschungshauptwerkstatt, denen wir den Bau der Zellen verdanken. Wolf möchte ich besonders für die Mühe und Geduld, die er mit und für uns hatte, sowie für die schnelle Bearbeitung unserer Wünsche danken. Bei technischen Problemen jedweder Art, sowie mit der High-Speed-Kamera im speziellen, standen mir Thomas Eggers und Kristian Hantke einmalig hilfsbereit zur Seite - teilweise obwohl es Freitagabend war und sie eigentlich schon längst zu Hause, beziehungsweise im Zug, sein sollten.
Zuletzt möchte ich meinem Freund Leon danken, der mir nicht nur seine Kameras geliehen hat, sondern meistens/manchmal auch Verständnis für meine schwankenden Launen während der Endphase der Arbeit hatte.

Erklärung

Erklärung nach §13 Abs. 8 der Prüfungsordnung für den Bachelor-Studiengang Physik und den Master-Studiengang Physik an der Universität Göttingen:
Hiermit erkläre ich, dass ich diese Abschlussarbeit selbständig verfasst habe, keine anderen als die angegebenen Quellen und Hilfsmittel benutzt habe und alle Stellen, die wörtlich oder sinngemäß aus veröffentlichten Schriften entnommen wurden, als solche kenntlich gemacht habe.
Darüberhinaus erkläre ich, dass diese Abschlussarbeit nicht, auch nicht auszugsweise, im Rahmen einer nichtbestandenen Prüfung an dieser oder einer anderen Hochschule eingereicht wurde.

Göttingen, den 08. September 2014

(Sonka Reimers)